Science
AAAS

Supplementary Materials for

SOX9 switch links regeneration to fibrosis at the single-cell level in mammalian kidneys

Shikhar Aggarwal *et al.*

Corresponding author: Sanjeev Kumar, Sanjeev.Kumar@cshs.org

DOI: 10.1126/science.add6371

The PDF file includes:

Other Supplementary Material for this manuscript includes the following:

Materials and Methods

All surgical procedures, and all mouse handling and husbandry were performed according to guidelines issued by the Institutional Animal Care and Use Committees (IACUC) at Cedars Sinai Medical Center and were performed after approval from institution's IACUC committee. Institutional IRB approved human kidney biopsies were utilized for immunostaining studies.

Mouse strains

The animals used in the study are detailed in table S4.

All mice were on a C57BL/6 background except $WI^{fl/fl}$. The wild-type C57BL/6 mice were obtained from Charles River, MA (USA). Only adult male Cre-drivers were used to generate Cre containing animals. $Sox9^{IRES\text{-}CreERT2/+}$ (*58*), $Axin2^{CreERT2/+}$, $Pdgfr\text{-}b^{CreERT2/+}$ mice, were crossed with reporter $R26R^{tdTomato/tdTomato}$ (hereafter referred to as $R26R^{tdT/tdT}$) mice to obtain corresponding $Sox9^{IRES\text{-}CreERT2/+}$: $R26R^{tdT/+}$, $Axin2^{CreERT2/+}$: $R26R^{tdT/+}$, $Pdgfr\text{-}b^{CreERT2/+}$: $R26R^{tdT/+}$ mice for lineage tracing studies. $Sox9^{IRES\text{-}CreERT2/+}$: $R26R^{tdT/+}$, $Axin2^{CreERT2/+}$: $R26R^{tdT/+}$ $Pdgfr\text{-}b^{CreERT2/+}$: $R26R^{tdT/+}$ mice, respectively, were crossed with reporter : *Acta2-GFP* mice (*59, 60*) to obtain corresponding $Sox9^{IRES\text{-}CreERT2/+}$: $R26R^{tdT/+}$: *Acta2-GFP*, $Axin2^{CreERT2/+}$: $R26R^{tdT/+}$: *Acta2-GFP*, $Pdgfr\text{-}b^{CreERT2/+}$: $R26R^{tdT/+}$: *Acta2-GFP* to ascertain the spatiotemporal relationship of the lineages with $Acta2\text{-}GFP^{+}$ myofibroblast populations. $Axin2^{CreERT2/+}$ mice were crossed with reporter $R26R^{mTmG/mTmG}$ (hereafter referred to as $R26R^{mTmG/+}$) mice to obtain $Axin2^{CreERT2/+}$: $R26R^{mTmG/+}$ mice for lineage tracing studies. To label uninjured, normal adult proximal tubular epithelial cells, $Slc34a1^{CreERT2/+}$ mice were crossed with $R26R^{tdT/tdT}$ animals to obtain $Slc34a1^{CreERT2/+}$: $R26R^{tdT/+}$ animals. To generate tamoxifen-inducible, Acta2-specific, b-catenin knock-out mice that also enabled scrutiny of cells with successful recombination, first, $Ctnnb1^{fl/fl}$: $R26R^{tdT/tdT}$ mice were obtained via breeding $Ctnnb1^{fl/fl}$ crossed to $R26R^{tdT/tdT}$. $Acta2^{CreER/+}$: $Ctnnb1^{fl/+}$: $R26R^{tdT/+}$ were then obtained by crossing $Acta2^{CreER/+}$ (*61*) to $Ctnnb1^{fl/fl}$: $R26R^{tdT/tdT}$. $Acta2^{CreER/+}$: $Ctnnb1^{fl/+}$: $R26R^{tdT/+}$ were bred with $Ctnnb1^{fl/fl}$: $R26R^{tdT/tdT}$ animals to generate $Acta2^{CreER/+}$;$Ctnnb1^{fl/fl}$;$R26R^{tdT/+}$ knock-out animals. The $Acta2^{CreER/+}$: $Ctnnb1^{+/+}$: $R26R^{tdT/+}$ served as controls. On similar lines, $Sox9^{IRES\text{-}CreERT2/+}$: $WIs^{fl/fl}$: $R26R^{tdT/+}$ (Sox9-cell specific Wntless knock out mice) and $Sox9^{IRES\text{-}CreERT2/+}$; $Wntless^{fl/+}$;$R26R^{tdT/+}$ control animals were generated. Here, the control animals retained a single active *Wntless* allele, as controls (SOX9:*WIs*-Het). Similar breeding strategy was employed to obtain *LyzM*-lineage specific, *WIs*-cKO (*LyzM*Cre;$WI^{fl/fl}$;$R26R^{tdT/+}$) animals and corresponding wild-type control animals (*LyzM*Cre;$WIs^{+/+}$;$R26R^{tdT/+}$).

To generate doxycycline-inducible, nephron epithelia specific Sox9 knock-out mice which will also enable demarcation of cells with successful recombination, $Sox9^{fl/fl}$: $R26R^{tdT/tdT}$ mice were obtained via breeding $Sox9^{fl/fl}$ crossed to $R26R^{tdT/tdT}$ and $Pax8^{rTA}$:$tetO^{Cre}$ animals were generated by crossing $Pax8^{rTA}$ and $tetO^{Cre}$ animals. $Sox9^{fl/fl}$: $R26R^{tdT/tdT}$ were bred to $Pax8^{rTA}$:$tetO^{Cre}$ animals to generate $Pax8^{rtTA}$:$tetO^{Cre}$;$Sox9^{fl/+}$;$R26R^{tdT/+}$ animals. The progeny crossed to $Sox9^{fl/fl}$: $R26R^{tdT/tdT}$ to generate $Pax8^{rtTA}$:$tetO^{Cre}$:$Sox9^{fl/fl}$:$R26R^{tdT/+}$ (Sox9 conditional knock out) and $Pax8^{rtTA}$;$tetO^{Cre}$;$Sox9^{+/+}$;$R26R^{tdT/+}$ (control, Sox9-WT) animals.

For induction of CreERT2 protein, mice were injected with tamoxifen (Sigma, #T5648) dissolved in corn oil (Sigma, #C8267) via an intra-peritoneal (i.p.) route. Briefly, tamoxifen was dissolved in corn oil at 20 mg/ml by continuous stirring in a glass silver-foil wrapped scintillation vial on a heated platform at 42°C for 2 hours. The stock solution (20mg/ml) was stored at 4°C for no more

than one week. Prior to administration, tamoxifen solution was warmed for 10 min at 37°C. The dosing schedule, frequency, and timing of the administration are documented in the results. All animals underwent tamoxifen, 2 mg/injection unless otherwise stated.
For induction of doxycycline-inducible Cre protein, mice were injected with doxycycline (Sigma, #T5648) dissolved in 0.9% normal saline via an intra-peritoneal (i.p.) route. The dosing schedule, frequency, and timing of the administration are documented in the results. All animals underwent doxycycline, 2 mg/injection unless otherwise stated.

Acute kidney injury to chronic kidney disease models
Ischemia reperfusion injury-induced AKI model: Age- (9 – 12 weeks old) and weight –matched male (25 – 30 g) male mice were subjected to bilateral renal ischemia reperfusion injury (IRI) surgery as previously described *(5, 10)* . Briefly, mice were anesthetized with an intraperitoneal injection of ketamine/xylazine cocktail. The kidneys were approached via a midline abdominal incision, and both the renal pedicles were clamped for 19 minutes using non-traumatic microaneurysm clamps (Roboz Surgical Instrument Co.). A return to their original color after removal of the clamps indicated successful restoration of the blood flow. Sham-operated mice underwent a similar surgical intervention except for the clamping of the renal pedicles. The body temperature was maintained at 36°C throughout the procedure. The mice were euthanized at the desired study end-point. All surgeries were conducted between 2 pm and 7:30 pm.
Rhabdomyolysis injury-induced AKI model: Briefly, adult male mice (25 – 30 g, 9-12 weeks old) were anesthetized with an intraperitoneal injection of ketamine/xylazine cocktail, and AKI was induced by intramuscular injection of 50% hypertonic glycerol solution (Sigma) in phosphate buffered saline (PBS), injected in each quadriceps muscle of mice using insulin syringe (total dose, 8 mg/kg). Animals were euthanized at the desired study end-point.

Serum creatinine analysis
Serum creatinine levels were measured at the UAB-UCSD O'Brien Center, UAB Biochemical Genetics and Metabolic Disease Laboratory (University of Alabama at Birmingham, USA) using an automated blood analyzer.

Mouse primary renal cortex epithelial cell culture
C57BL/6J adult (10- to 12-week-old) male mice were euthanized as per the approved IACUC protocol and immediately perfused with cold PBS through the left heart ventricle. Kidneys were excised and placed in cold PBS in a 6 mm petri dish on ice for immediate processing. Kidney capsules were removed using sterile fine forceps. Cortices were dissected and thoroughly minced in warm DMEM/F12 medium using sterile fine forceps. The minced tissue was transferred to a nuclease-free 15 ml conical tube and resuspended in fresh 3 ml warm DMEM/F12 medium supplemented with 150 mg/ml Liberase TL (Roche), and incubated at 37^0C with continuous orbital shaking at 160 rpm. Tissue suspension was mixed by pipetting with a 1 mL pipette every 10 minutes until tissues were completely dissociated to form a single cell suspension. The enzymatic reaction was stopped using DMEM/F12 medium + 10% Fetal Bovine Serum. Cell suspension. Subsequently, the cell suspension was filtered through a 40 μm cell strainer (BD Biosciences). The filtrate was then centrifuged at 300 *g* for 5 min at 4^0 C, and the pellet was resuspended in DMEM/F12 medium + 10% FBS. For confluency experiments, 2 million cells/well were transferred to a 6-well plate followed by a medium change after 48 hours. For sub confluent (40 – 50% confluency) and confluent (95 – 100%, tight monolayer formation) analyses, cells were

collected at day 4 and day 7, respectively. A day before harvesting confluent cells, the cells were serum starved for 24 hours.

Human primary renal proximal tubular epithelia cells (ATCC #PCS-400-010), cultured in renal epithelial cell basal medium (ATCC #PCS-400-030) supplemented with renal epithelial cell growth kit (ATCC #PCS-400-040), at 37°C, 5% CO_2 were cultured to either sub-confluent (40 – 50% confluency) or confluent (95 – 100%, tight monolayer formation) state.

In vitro recombination cell experiment

For in vitro recombination, 1.3 µM 4OH-TAM (Sigma-Aldrich #H7904) or equal volume of vehicle (methanol) was administered to cells 48 hours after isolation. Cells were analyzed 48 hours post treatment.

Bone marrow macrophage

For in vitro validation of *LyzM*Cre;$WI^{fl/fl}$;$R26R^{tdT/+}$ knock out mice, bone marrow cells were flushed from femurs and tibiae of *LyzM*Cre;$WI^{fl/fl}$;$R26R^{tdT/+}$ knock out or *LyzM*Cre;$WI^{+/+}$;$R26R^{tdT/+}$ control mice using cold RPMI-1640 (Corning #10-041-CV) and 31G needle-syringe (BD). Cells were passed through syringe multiple times followed by a 70 µm cell strainer (Fisher Scientific #08-771-2) to obtain a single cell suspension, washed, and counted. Cells were then seeded at a density of 2 x 10^6 per well of a 6-well plate (Nunc #140675) and were cultured in complete RPMI-1640, supplemented with 10% fetal bovine serum, 1x penicillin-streptomycin (Millipore Sigma #P4333), and 50 ng/ml recombinant human M-CSF (PeproTech #300-25). On day 4, culture medium was changed with fresh complete medium, and cells were collected by trypsinization after 7 days of culture and used for assays.

Masson's Trichrome (MTC) staining

Mouse kidneys were perfused with ice-cold PBS and fixed overnight in 4% paraformaldehyde (PFA) at 4°C. Tissues were processed and embedded in paraffin using Leica ASP300S machine according to the routine histology protocols. 4 µm thick paraffin sections were cut using Leica RM2255 machine and slides containing tissue sections were stained for MTC staining as per standard protocols. Briefly, tissue sections were deparaffinized by incubating at 60°C for 1 hour and subjected to serial order of Xylene and decreasing ethanol concentration (100% to 50%) for 5 min each step. Slides were washed in water and incubated for 1 hour in Bouin solution at 60°C. Slides were then cooled to room temperature, washed with running water and 1% Ammonium hydroxide in 70% ethanol. Slides were then incubated with different staining solutions serially with Weigert's Hematoxylin (10 min), Biebrich Scarlet-Fuchsin acid solution (2 min), Phosphomolybdic acid solution (12 min), Aniline blue in acetic acid (8 min) and washed with running water after each step. All chemicals were purchased from Sigma. Slides were dehydrated and mounted with mounting medium (Richard-Allan Scientific #4112) and dried overnight under the chemical hood. Images were acquired using slide scanner (Zeiss Axioscan.Z1).

Analysis, co-immunoanalysis and histological evaluation of renal fibrosis

The degree of interstitial fibrosis was evaluated by a board-certified renal pathologist (MY) in a blinded manner on Masson's trichrome-stained slides as follows: 0: <5% fibrosis, 0.5: 5% to 10% fibrosis, 1: 10% to 25% fibrosis, 2: 25% to 50% fibrosis, and 3: >50% fibrosis. All the study animals were coded, and all data were generated using at least n=3 biological replicates unless

stated otherwise. The precise numbers of animals included in each group or intervention are stated in the respective legend section and no datapoints were excluded in the analysis. All the quantifications involving the coded control and knock out animals were conducted via a blinded analysis. Blinded whole scanned kidney images in certain instances, for example, from Sox9-Ctrl and Sox9-cKO animals were examined. It was ensured that the sections that contain the entire longitudinal section of the kidney highlighted by the presence of outer/inner medulla were interrogated. Such sections were randomly selected and random representative images of the regions were attained. Quantification that involved interrogation of cells of interest for example tdT^{pos} cells, random images were taken of fields containing such cells of interest. For Cdh6 negative lineage: Random images of the lineage-traced cells that were Cdh6 negative thus demarcating the $Sox9^{on\text{-}off}$ state (regenerated lineage, $tdT^{pos}Cdh6^{neg}$) were interrogated for adjacent aSMA myofibroblast response. Vice versa, $Sox9^{on\text{-}on}Cdh6^{pos}$ cells would highlight unresolved regenerated lineage. For comparing two independent groups, unpaired, 2-sided *Student's* t-test was utilized.

Kidney cell isolation for Fluorescence Activated Cell Sorting (FACS) and single-cell sequencing (modified cold enzymatic digestion protocol)

We modified the original published cold enzymatic digestion protocol (*62*) as follows:
Mice were euthanized as per the approved IACUC protocol and immediately perfused with cold PBS through left heart ventricle. Kidneys were then excised and placed in cold PBS in a 6 mm petri dish on ice for further processing. Kidney capsules were removed using sterile fine forceps. Cortices and outer medulla regions of the kidney were dissected and thoroughly minced in 1 ml cold DMEM/F12 medium using sterile fine forceps. The minced tissue was transferred to a nuclease-free 15 ml tube and resuspended in fresh 1ml DMEM/F12 medium supplemented with 7.5 mg/ml of *B. Licheniformis* Cold Active Protease (Creative enzymes), 125 U/ml DNase1 (Stem cell technologies) and 0.1mg/ml Liberase TL (Roche) and continuously kept on ice for 1 hour with frequent pipetting using 1 ml pipette every 10 min. After complete dissociation of tissues into single cells (an aliquot of cell suspension was taken every 20 min to check dissociation of the tissue under the microscope), the enzymatic reaction was stopped using cold DMEMF12 medium + 10% FBS. The cell suspension was filtered through a 40 μm cell strainer. The filtrate was then centrifuged at 300 *g* for 5 min and transferred to 5 ml Polystyrene Round-Bottom FACS tubes (BD Biosciences). Cells were washed in PBS and resuspended in 1.5 ml of FACS sorting buffer containing 1 mg/ml DAPI (1:1000, Life Technologies) or APC/Cyanine7 anti mouse F4/80 antibody (1:20, Biolegend #132118), when required. Cell sorting was performed using the FACSAria III cell sorter (BD Biosciences). Cell populations were gated to exclude debris and doublets using FACSDiva software (BD Biosciences). Cells were collected from relevant gated cell populations in 1.5mL collection tubes (Eppendorf) containing collection buffer. Sorted cells were immediately centrifuged at 300g for 10 minutes at 4 degrees Celsius. Cell pellets were resuspended in RLT buffer (Qiagen) for RNA isolation using RNeasy Micro Kit (Qiagen). FlowJo software (Tree Star) was used for further analysis and live cells were gated as DAPI negative population after excluding doublets using FSC-H and SSC-H gates.

shRNA lentiviral vectors and infection

Mouse *Sox9* shRNA vectors pLKO.1-sh-mSox9-5 (*28*) (Addgene #40646), non-hairpin control pLKO.1-TRC control (Addgene #10879), packaging vector psPAX2 (Addgene #12260) and envelope vector pMD2.G (Addgene #12259) were purchased from Addgene. shRNA vectors

pLKO.1-sh-mSox9-5 and pLKO.1-TRC plasmids were digested using BamHI (NEB #R3101S) and KpnI (NEB R3142S) to remove puromycin resistant gene and to insert eGFP reporter. Lentivirus Production: HEK293T cells (ATCC CRL-11268), cultured in DMEM supplemented with 10% FBS, at 37°C, 5% CO_2, were seeded at ~90% confluency in T-75 flask the day before transfection. On the day of transfection, 10.2 µg pLKO.1-shRNA plasmid, 7.8 µg psPAX2 plasmid and 5.1 µg pMD2.G plasmid were co-transfected into HEK293T cells using Transporter 5 transfection reagent (Polysciences #26008-5) according to the manufacturer's instructions. Medium was replaced 18 hours post transfection. Viral supernatant was harvested at 24, 48, and 72 hours post transfection, centrifuged, and filtrated through a 0.45 um filter. The filtrated viral supernatant was then concentrated using Lenti-X concentrator (Takara #631232) according to the manufacturer's instructions, aliquoted and stored in -80°C. Lentivirus Transduction: Before lentivirus transduction, mouse primary cells were cultured to ~30% confluency. On the day of transduction, the medium was changed to fresh DMEM/F-12 with 10% FBS containing 8 µg/mL polybrene and lentivirus (MOI=30). The second transduction was performed 24 hours post the first transduction. 24 hours post 2nd transduction, the cells were cultured in fresh medium and were ready for analysis 96 hours post 1st transduction.

Primers used for plasmid construction

Name	Sequence
BAMHI-EGFP-F	*TCCGGATCCACCGGAGCTTACCATGGTGAGCAAGGGC*
KPNI-EGFP-R	*ACCGGTACCTTACTTGTACAGCTCGTC*

Quantitative PCR

RNeasy Mini Kit (QIAGEN #74104) was used to isolate total RNA from cultured cells or RNAlater (Life Technologies #AM7020) preserved tissues. RNeasy Micro Kit (QIAGEN #74004) was used to isolate total RNA from FACS sorted cells. cDNAs were synthesized using SuperScript VILO cDNA Synthesis Kit (Life Technologies #11754050) according to the manufacturer's instructions. Quantitative PCR (qPCR) was performed using PowerUp SYBR Green Master Mix (Life Technologies #A25742) on a QuantStudio 3 real-time PCR system. For cultured cells or RNAlater preserved tissues, 5 ng of cDNA, and for sorted cells 0.25 ng cDNA was used in each reaction. For sorted cells, 0.25 ng cDNA was used in each reaction. See table S5 for primers used for qPCR.

Western Blot

Cells were homogenized in cold RIPA buffer (ThermoScientific #89900) supplemented with phosphatase inhibitors PhosStop tablet (Roche #04906837001), Complete protease inhibitor (Sigma #11697498001) and PMSF (Sigma #93482-50ml-F), directly in the cell culture dish on ice. The cell extract was then incubated on ice for 30 minutes with intermittent vortexing and then centrifuged at maximum speed of 14000 rpm for 12 minutes at 4°C. Supernatant containing proteins was collected and quantified using Pierce BCA protein estimation kit (Thermo Scientific). 15mg protein of interest was resuspended in 6X Laemmli SDS Sample buffer (Bioland Scientific LLC #SAB03-02), boiled for 5 min at 95°C and kept on ice for further processing. Proteins were separated by SDS-PAGE (Invitrogen) and transferred onto nitrocellulose membranes (0.2 mm, Biorad) overnight using wet transfer apparatus (Invitrogen). The membranes were blocked with 5% BSA (Sigma) in PBS for 2 hours at room temperature and detected using the primary antibodies against ACTB (1:1000, Cell Signaling Technology #4967S), SOX9 (1:1000, Abcam

#AB185230), and CDH6 (1:500, Sigma #HPA007047) diluted in 2.5% BSA in 0.1% PBS-Tween. All primary antibodies were incubated overnight at 4°C. All secondary antibodies were used at 1:3000 and incubated for 1 hour at room temperature. Freshly prepared SuperSignal West Pico Chemiluminescent Substrate (Thermo Scientific) was used to visualize the proteins simultaneously by Chemi / infrared detection using the Li-Cor Odyssey Imaging System. Bands were quantified with ImageJ software (NIH).

Immunofluorescence Staining

Ice-cold PBS perfused kidneys were fixed for 1.5 hours in 4% PFA (Santa Cruz #SC-281692) at 4 degree Celsius, incubated overnight in 30% sucrose in PBS and cryoblocked in OCT (VWR #25608-930). The cryoblocks were then sectioned to 6-micron sections using a Leica CM3050S Cryostat and mounted on Superfrost slides. Cryo sections were incubated with primary antibodies detailed in table S6.

At the day of IF staining, cryosections were brought to room temperature from -80 freezer and washed using PBS to remove OCT. The sections were then permeabilized using PBST (PBS with 0.1% Triton X-100) and blocked for 2 hours in blocking buffer (PBST with 3% BSA and 5% Donkey/Goat serum). After blocking, sections were incubated with primary antibodies diluted in blocking buffer at 4°C overnight. The next day, the sections were incubated with secondary antibodies at room temperature for 1 hour and then with 1 mg/ml DAPI in PBS for 10 minutes. Finally, the sections were mounted using fluorescence mounting medium (Agilent Technologies, #S302380) and sealed with nail polish (Electron Microscopy Sciences, #72180). Images were acquired using confocal (Carl Zeiss 780 LSM), and/or slide scanner (Zeiss Axioscan.Z1). Videos were acquired using confocal Leica Sp8 X microscope.

Secondary antibodies used in the study are detailed in table S7. Images were acquired using confocal (Carl Zeiss 780 LSM), and/or slide scanner (Zeiss Axioscan.Z1).

RNAscope

RNAscope based in situ hybridization (ISH) assay was performed on 12 µm cut kidney OCT-embedded cryosections following the RNAscope RNA-Protein Co-detection Ancillary Kit (Advanced cell diagnostics (ACD), Cat# 323180) and Multiplex Fluorescent Reagent Kit v2 kit (ACD, Cat# 323100) as per the kit protocol (document number: MK51-150 TN and document number: 323100-USM). Briefly, cryosections (12 µm) were taken out from -80°C freezer and fixed with fresh 4% PFA overnight at 4°C. Next day, sections were processed with alcohol-gradient based dehydration and antigen retrieval steps and incubated with primary antibody of interest overnight at 4°C after the pretreatment steps. The following day, sections were washed with PBS and incubated with specific probes for 2 hours. *Sox9*-C1 probe was used as diluent for *Wnt4*-C2 (1:75), and *Bmp4*-C2 (1:50). RNAscope Multiplex fluorescent v2 assay protocol was followed hereafter for the development of fluorescent signal and the signal for RNA was detected using 1:750 dilution of Opal dyes-570 (Akoya Biosciences; cat# FP1488001KT) and Opal dyes-690 (Akoya Biosciences; cat# FP1497001KT) for the respective C1 or C2 probe channel. Thereafter, sections were incubated with Alexa Fluor conjugated secondary antibody-488 (ThermoFisherScientific) for the antibody co-detection. The negative control (without any RNA probe) and the positive control *Slc12a3* was treated with the similar protocol (but without antibody detection) and run alongside the experimental sections. RNA probes were purchased from ACD. Transcript quantifications in the images was performed using the 'spots' algorithm of the Bitplane Imaris 9.3.1. software. Briefly, diameter was chosen for each spot using the 'spots' algorithm and

applied automatically to each image with a set threshold and the total number of spots per image per volume were quantified per channel. It was then normalized to the number of DAPI positive nuclei quantified with the same algorithm in the same image and presented as the average of 12-15 images per mice in each group.

Bulk-RNA sequencing and bioinformatics analysis

Library construction was performed using Universal plus mRNA-seq with NuQuant kit from NuGEN. Briefly, total RNA samples were assessed for concentration using a Nanodrop (Nanodrop ND8000, Thermo Fisher Scientific, Carlsbad, CA) and quality using the TapeStation (4200 TapeStation, Agilent Technologies, Santa Clara, CA). Up to 30 ng of total RNA per sample was used for poly-A mRNA selection. Libraries for RNA-Seq were prepared with Nugen Universal plus mRNA-Seq Kit (part number: 0508) to generate strand-specific RNA-seq libraries. The workflow consists of poly(A) RNA selection, RNA fragmentation and double-stranded cDNA generation using a mixture of random and oligo(dT) priming, followed by end repair to generate blunt ends, adaptor ligation, strand selection, and PCR amplification to produce the final library. Different index adaptors were used for multiplexing samples in one sequencing lane. The concentration of the amplified library was measured with a Qubit fluorometer and an aliquot of the library was resolved on a Bioanalyzer. Sample libraries are multiplexed and sequenced on a NovaSeq GAP 285 platform (Illumina) using 150 bp paired-end sequencing. On average, about 30 million reads were generated from each sample. Data quality check was done on Illumina SAV. Demultiplexing was performed with Illumina Bcl2fastq2 v 2.19.1.403 program.

Bioinformatic analysis of RNA-seq of FACS sorted, labeled kidney cell-types

Raw sequencing data was demultiplexed and converted to fastq format by using bcl2fastq v2.20 (Illumina, San Diego, CA). Then reads were aligned to the transcriptome using STAR (version 2.6.1) (*63*)/ RSEM (version 1.2.28) with default parameters, using a custom MOUSE GRCh38 transcriptome reference downloaded from http://www.gencodegenes.org, containing all protein coding and long non-coding RNA genes based on MOUSE GENCODE version 33 annotation. Expression counts for each gene in all samples were normalized by a modified trimmed mean of the M-values normalization method and the unsupervised PC analysis (PCA) was performed with DESeq2 Bioconductor package version 1.26.0 in R version 3.6.3. Each gene was fitted into a negative binomial generalized linear model, and the Wald test was applied to assess the differential expressions between two sample groups by DESeq2. Benjamini and Hochberg procedure was applied to adjust for multiple hypothesis testing, and differential expression gene candidates were selected with a false discovery rate less than 0.05. Further filtering of candidate differentially expressed genes to false discovery rate less than 0.01 and an absolute log 2-fold-change greater than 1 was applied to the studies comparing normal uninjured PTEC vs. Sox9:48h IRI vs. Sox9: day14 post IRI. GO term enrichment was conducted with DAVID retaining only terms with a p-value for enrichment less than 0.01. After manually merging redundant biological process GO terms, relevant terms among the top 20 were plotted using custom scripts in R and the ggplot2 (version 3.3.3) package. For visualization of coordinated gene expression in samples, a two-way hierarchical clustering with Pearson correlation distance matrix was performed with samples and DEG candidates using the Bioconductor g-plots package (version 3.0.3) in R. MA plots, and PCA plots were created using custom R scripts and the Bioconductor FactoMineR package (version 2.4).

Bioinformatic analysis of single cell RNA-sequencing

Sequencing library construction using the Chromium platform: Single-cell RNA-Seq libraries were prepared per the Single Cell 3′ v3 Reagent Kits User Guide (10X Genomics, Pleasanton, California). Cellular suspensions were loaded on a Chromium Controller instrument (10X Genomics) to generate single-cell Gel Bead-In-EMulsions (GEMs). GEM-RT was performed in a Veriti 96-well thermal cycler (Thermo Fisher Scientific, Waltham, MA). GEMs were then harvested, and the cDNA amplified and cleaned up with SPRIselect Reagent Kit (Beckman Coulter, Brea, CA). Indexed sequencing libraries were constructed using Chromium Single-Cell 3′ Library Kit for enzymatic fragmentation, end-repair, A-tailing, adapter ligation, ligation cleanup, sample index PCR, and PCR cleanup. The barcoded sequencing libraries were quantified by quantitative PCR using the KAPA Library Quantification Kit for Illumina platforms (KAPA Biosystems, Wilmington, MA). Sequencing libraries were loaded on a NextSeq500 (Illumina, San Diego, CA) with a custom sequencing setting (26bp for Read 1 and 98bp for Read 2) to obtain a sequencing depth of ~200K reads per cell.

Data analysis: Raw sequencing data was demultiplexed and converted to FASTQ format using bcl2fastq v2.20. Cell Ranger v6.0.2 (10X Genomics) was used for barcode identification, read alignment, and UMI quantification with default parameters and aligning to the mouse reference genome GRCm38. In addition to the empty droplet filtering performed by Cell Ranger, poor-quality cells were removed by setting a maximum mitochondrial read percent (35%), minimum UMI count (1000), and an acceptable range of detected genes (min 300, max 7000). The samples were integrated together with Seurat v4.0.5 (*64*) in R v4.1.1 using the functions SCTransform() followed by FindIntegrationAnchors(). To obtain two-dimensional projections of the population's dynamics, principal component analysis (PCA) was run on the SCTransformed gene-barcode matrix to reduce the number of feature dimensions. After running PCA, both UMAP and tSNE algorithms were applied on the top 20 principal components to further reduce these components and to visualize cells in a two-dimensional space. Following Louvain clustering of the cells, cell types were identified based on expression of known marker genes for kidney cell types. Clusters without common marker gene expression were annotated by mapping orthologous gene expression to the Azimuth Kidney reference (*64, 65*). Differential expression analysis were conducted with Seurat using the function FindMarkers() on the normalized RNA expression matrix. Subsequent GO enrichment analysis were conducted using the R package ClusterProfileR (*66*) with term annotations drawn from the R package org.Mm.eg.db. Single-cell tSNE and UMAP embeddings GO enrichment plots were created with custom R scripts.

Human Renal allograft RNA-seq.

Genome-wide gene expression profiling using RNA-seq was performed in kidney allograft recipients as previously described (*48, 49*) . Briefly, 42 patients were enrolled at the University Hospitals of Leuven. Protocol biopsies were performed at four different time points: before implantation (kidney flushed and stored in ice), after reperfusion (at the end of the surgical procedure) and 3 and 12 months after transplantation. The library was prepared with Clontech SMARTer technology at the Genome Technology Access Center of the Washington University (St. Louis, Missouri, USA). The sequencing was performed in the same laboratory using the HiSeq 3000 system on the Illumina platform, with a target of 30 M reads per sample. The reads were

aligned to the Ensembl top-level assembly with STAR version 2.0.4b. Gene correlation analysis, linear regression analysis and group comparisons were performed with Prism 9, Graphpad.

Analysis of published single-nuclear RNA-Seq (snRNA-Seq)

snRNA-Seq data were obtained from datasets previously described (*17, 18*). Seurat v3.2.0 in R v4 was used for analyses, including normalization, scaling, and clustering of nuclei. First, we analyzed each data set separately and excluded nuclei with fewer than 150 or more than 8000 genes detected. We also excluded nuclei with a relatively high percentage of unique molecular identifiers mapped to mitochondrial genes (>1) and ribosomal genes (>1, for normal kidney sample; and >2, all other samples). We performed curated doublet removal based on known lineage-specific markers. The samples from different data sets were integrated to avoid batch effect using Seurat standard workflow splitting by data set. Following ScaleData, RunPCA, FindNeighbours, and FindCluster at a resolution of 0.5 were performed and cluster annotated based on standard markers. We focused our analysis on the proximal tubular compartment selecting 4 h, 12 h, 48 h, 64 h, and 14 day time points, which are covering the time points 48 h and 10 days extensively characterized in this paper. For data visualization, we used RunUMAP and FeaturePlot from Seurat. Trajectory analysis was performed using Slingshot setting *PT* cluster as staring point.

Single nuclei ATAC sequencing

TdTomato positive enriched sorted cells were processed following the manufacture instruction. Sorted cells nuclei were isolated as described in 10xGenomics protocol (CG000169 Nuclei Isolation for Single Cell ATAC Sequencing), following the low input version and with a 1:5 diluted Lysis Buffer in Nuclease-free water. Isolated cell samples were immediately processed with a Chromium Next GEM Single Cell ATAC Kit v2 (10xGenomics).

Bioinformatic processing

TdT+ filtered peak matrices were generated at the Genomic Core at Cedars-Sinai with Cell Ranger. Datasets were analyzed with ArchR (*67*) and plots were postprocessed with ggplot2. In brief, the summarized pipeline consisted in datasets quality check and basic filters were applied filtering doublets and cells considered of bad quality (low TSS enrichment and or number of fragments based on a combined bidimensional threshold function). For dimensional reduction and bach corrections iterative LSI and Harmony algorithms were applied with UMAP embedding generated over the harmony-derived matrix. Preliminary clustering was generated by graph-based clustering and cluster marker gene tested with Wilcoxon statistic approach. Chromatin accessibility enrichment was denoised by weight imputation based on Markov affinity-based graph imputation of cells diffusion matrix (*68*) . Low quality clusters were filtered, and remaining cells reprocessed. Integration with scRNAseq datasets was used to define a preliminary cell type clustering which was refined based in the internal clustering of the scATACseq datasets. MACS2 was used for calling peaks and motif enrichment was defined using the CisBP motif set and chromVAR package (*69*) . A supervised trajectory analysis (defined by the unsupervised trajectory determined in the scRNAseq datasets) was calculated and integrative pseudo-time analyses were carried out with the default parameters in ArchR in a subset of the snATACseq dataset corresponding to the $Sox^{On\text{-}On}$ population lineage.

CUT&RUN genomic occupancy assay

Cells pellets of around 100.000 cells from 2 or 10 days post injury were lightly fixed in 0.2% PFA and frozen at –80 for storage until all samples were collected. Each sample was split into 3 aliquots to be processed with a Sox9 antibody (#AB5535, Millipore), as a positive control with H3K4me3 (#9751, Cell Signaling) or as an input control. CUT&RUN assays were carried out with the Cell Signaling assay kit and protocol (Catalog number #86652, Cell Signaling) and next-generation sequencing libraries were generated from the immuno-enriched DNA samples using the DNA Library Prep Kit for Illumina with the Multiplex Oligos for Illumina Systems (Dual Index Primers) kits (#56795 and #47538, Cell Signaling, respectively). The final library quality was assessed by fragment size in a TapeStation before sequencing.

Bioinformatic processing

Libraries were analyzed with Partek Flow software v10. In brief, unaligned reads were filtered out of contaminants using default parameter in the Filter contaminants (Bowtie 2) -2.2.5 Partek task and then aligned with the Bowtie 2.0.0 algorithm. Peaks calling was carried out using MACS3 using the input datasets as background peaks and a Cutoff q-value of 0.01 and the mm10 mouse genome version, additionally, scale was adjusted to the larger dataset in the Partek parameters for the MACS3 algorithm. Genomic regions were quantified with the defaults parameter in Partek flow and normalized to transcripts per million counts in each library to explore the samples with PCA analysis accounting by feature variability. Differential region enrichment was analyzed with Partek Flow's version of the GSA algorithm. Motif enrichment was studied within the positively enriched regions of the GSA analysis at 10 and 2 days against the JASPAR vertebrate database of binding motifs with a following manual curation of transcript factor motifs present in mouse. The enriched genesets between 48 hours and 10 days Sox9 CUT&RUN datasets were used for pathway analysis against the Gene Ontology (GO) database on Partek. Expression of significatively enriched GO pathway terms gene sets was cross analyzed in the scRNAseq datasets between 48 hours and 10 days samples using Seurat software, genes included in the subsequent GO pathway heatmap were filtered by adjusted p value < 0.05.

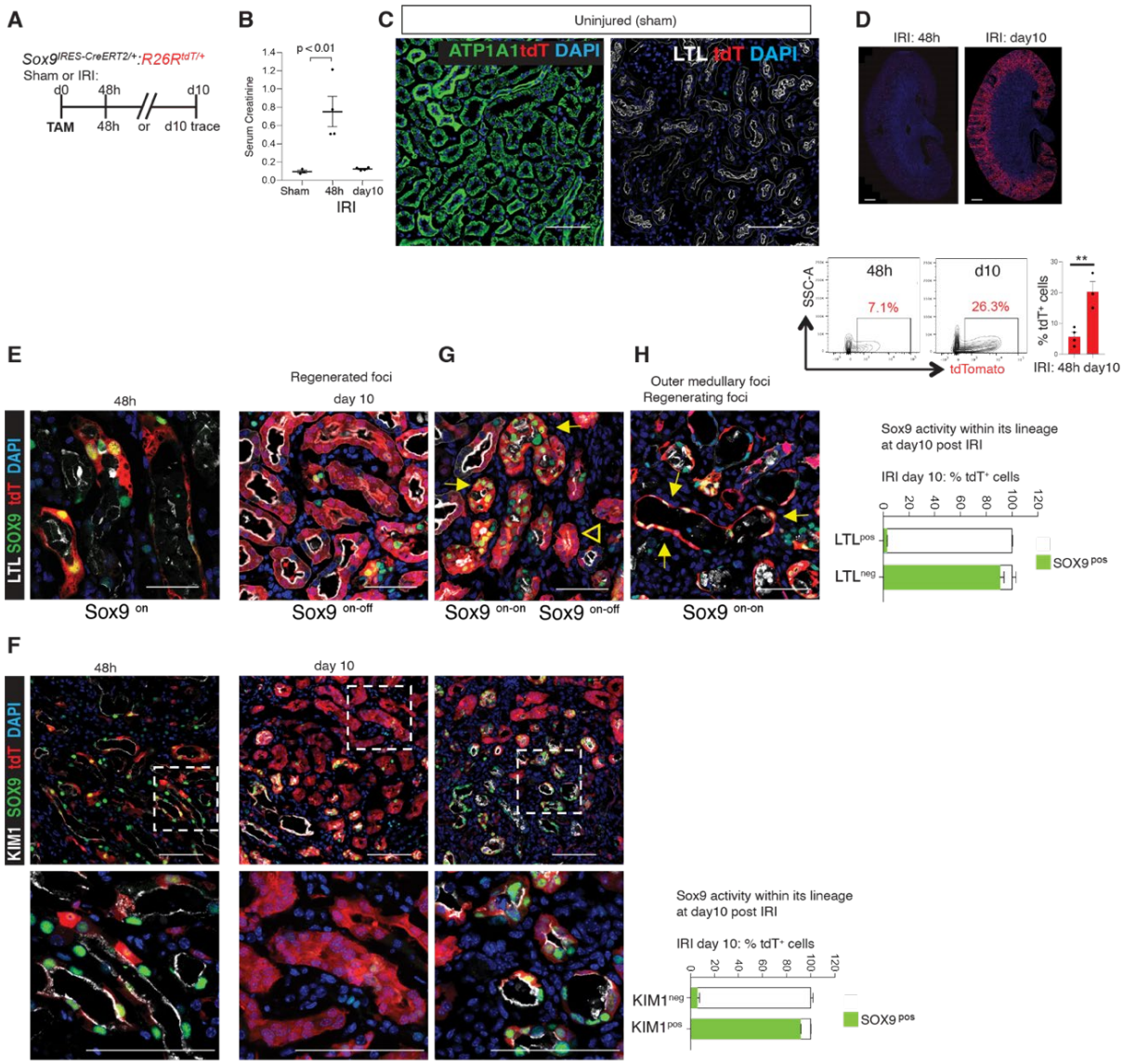

Figure S1. Identification of a dynamic Sox9 switch that parallels restorative status of its lineage post IRI-AKI.
(A) Schema of lineage-tracing of Sox9^{pos} cells after sham or renal IRI-induced AKI.
(B) Serum creatinine levels showing significant renal function dysfunction ($p < 0.01$) at 48h post-IRI with return to baseline by day10.
(C) Co-immunoanalysis for SOX9, ATP1A1 (NaKATPase), and proximal tubule (PT)-specific apical brush border marker LTL (lotus teragonolobus lectin) in post-sham surgery (uninjured kidneys) showing normal expression pattern of ATP1A1 and LTL.
(D) Representative whole scanned kidneys and FACS plot showing expansion of the initially labeled Sox9^{pos} cells by day10 post-IRI. **$p < 0.01$, unpaired, 2-sided, Student's t-test. Mean ± SEM. Scale bars: 1000μm.
(E) Co-immunoanalysis for SOX9 and LTL showing cells with disrupted apical brush border activated SOX9, the latter co-localized with tdT^{pos} cells at 48h after IRI. At day10 post-IRI, the Sox9-lineage that restored apical brush border silenced SOX9 (regenerated epithelia; Sox9$^{on\text{-}off}$ cells), whilst the lineage with unrestored apical polarity maintained SOX9 expression (Sox9$^{on\text{-}on}$ cells).
(F) Co-immunoanalysis for SOX9 and initial injury marker KIM1 (*Havcr1* encodes kidney injury molecule1) showing SOX9 activation within KIM1^{+} cells at 48h post-IRI. At day10, the Sox9-lineage that attained KIM1^{neg} status silenced SOX9, whilst subset of KIM1^{+} Sox9-lineage maintained SOX9 expression (Sox9$^{on\text{-}on}$ cells).
(G, H) Arrows pointing to different morphologies of Sox9$^{on\text{-}on}$ cells: clusters (arrows, G) and cells with filopodia lining the tubules (arrows, **H**). Arrows and arrowhead, highlighting Sox9$^{on\text{-}on}$ and Sox9$^{on\text{-}off}$ status, respectively, within the same initially injured foci (**G**).
Scale bars: 100μm. For total cells counted, see table S2.

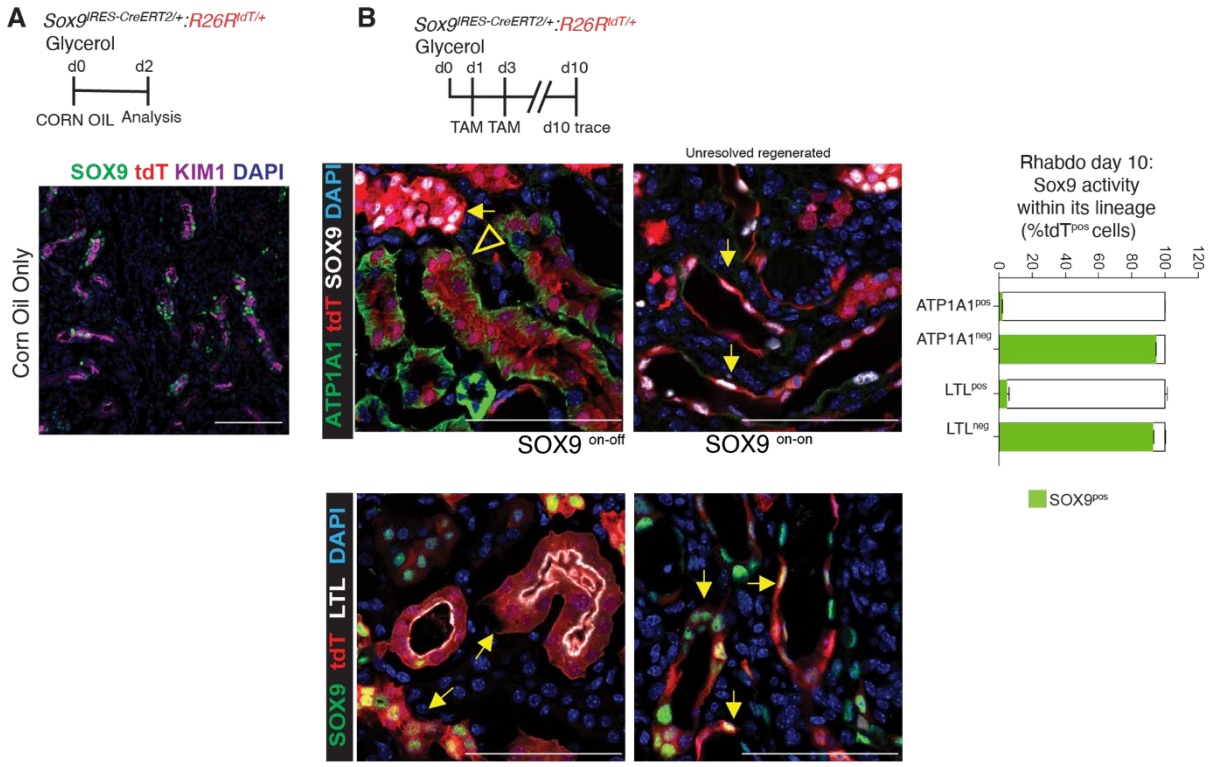

Figure S2. Injury-induced Sox9 lineage displays dynamic Sox9 switch after rhabdomyolysis induced AKI.

(A) Schema of corn oil injection after rhabdomyolysis-induced AKI and co-immunostaining for SOX9 and KIM1 showing no tdT^{pos} cells in corn oil only administered animals after rhabdo-AKI ruled out spontaneous injury-induced Cre activation, therefore, confirmed tamoxifen dependence in the setting of rhabdo-AKI.
(B) Identification of Sox9$^{on\text{-}off}$ and Sox9$^{on\text{-}on}$ cells post rhabdo-AKI:
Schema of lineage-tracing cells that activated SOX9 post rhabdo-AKI. At day10 post glycerol injection, the Sox9-lineage that restored apico-basolateral polarity silenced SOX9 (arrowhead, SOX9^{neg}tdT^{pos}, Sox9-derived regenerated epithelia; Sox9$^{on\text{-}off}$ cells), whilst the lineage with unrestored polarity maintained SOX9 expression, marking cells with sustained Sox9 activity (arrows, SOX9^{pos}tdT^{pos}; Sox9$^{on\text{-}on}$ cells). For total cells counted, see table S2. n=3 animals/time-point. Scale bars: 100μm.

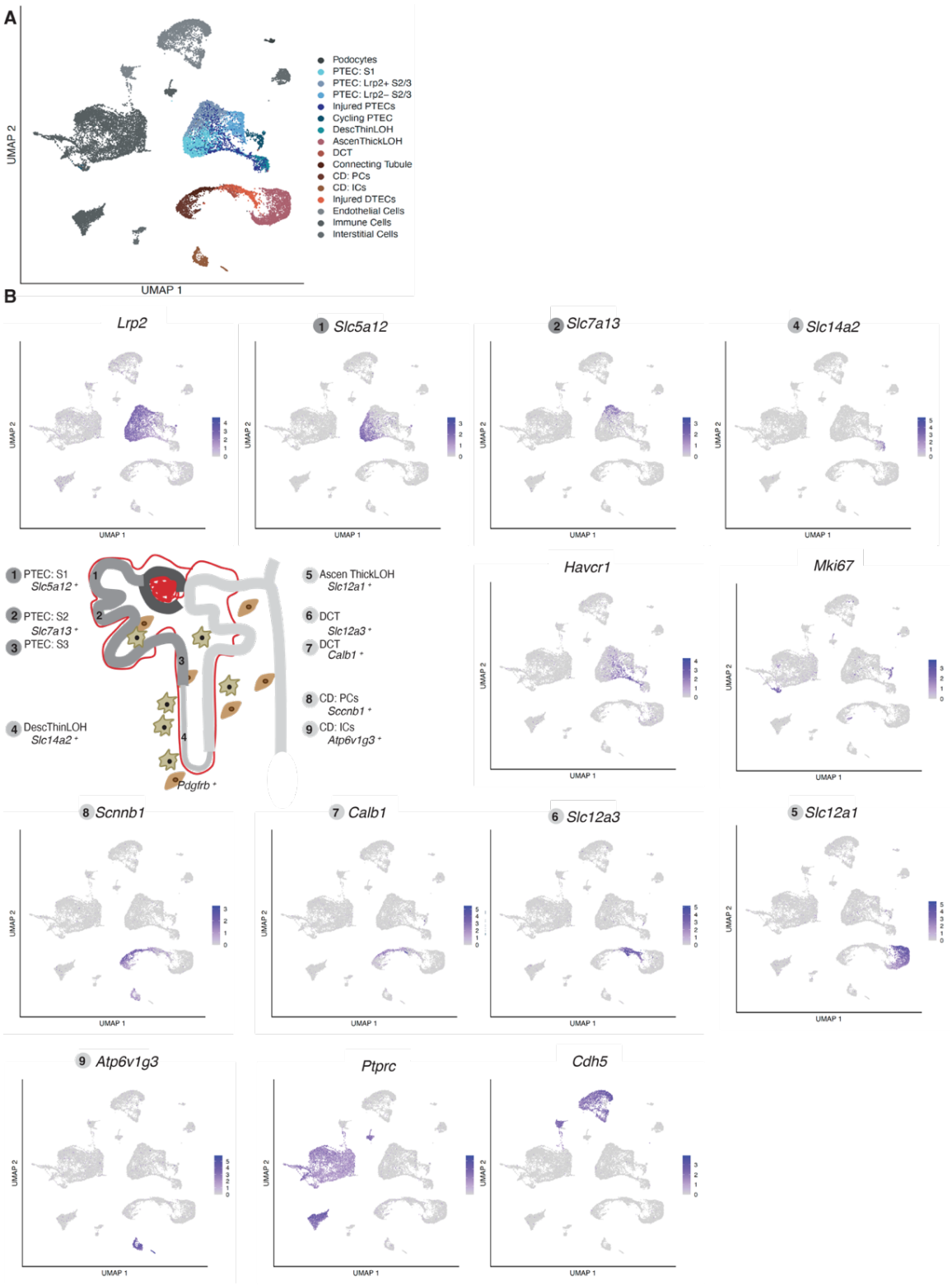

Figure S3. scRNA-seq analysis demonstrating distinct cell-types in the acutely injured kidneys.
(A) UMAP projection of kidney cells post IRI-induced AKI showing major clusters including distinct clustering of podocytes, immune, endothelial, and interstitial cell-types.
(B) UMAP projection of distinct kidney cell-types based on known canonical markers.
See **fig. S11** for *Pdgfrb* ^{pos} cluster.

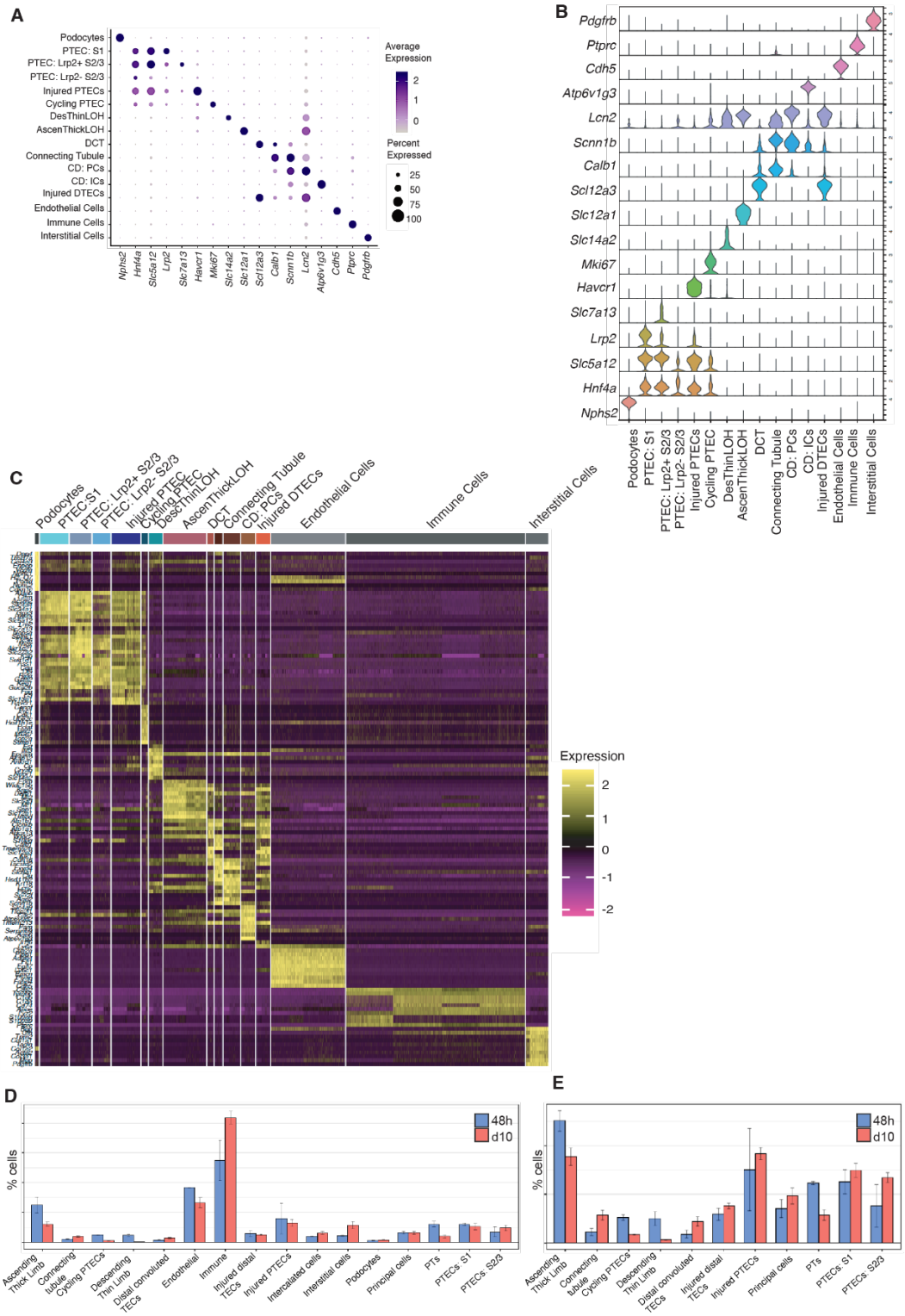

Figure S4. Characterization of single-cell RNA-seq analysis post ischemia reperfusion injury induced acute kidney injury.

(A, B) Dot plot (**A**) and violin plot (**B**) analysis of signature genes representing each major cluster.

(C) Heatmap of expression profiles of the top 10 most enriched genes within each identified cluster.

(D) Barplots showing cell count proportions within the complete datasets at 48h and day10, respectively, after injury.

(E) Barplots showing cell count proportions after removing non-epithelial cell types at 48h and day10, respectively, after injury.

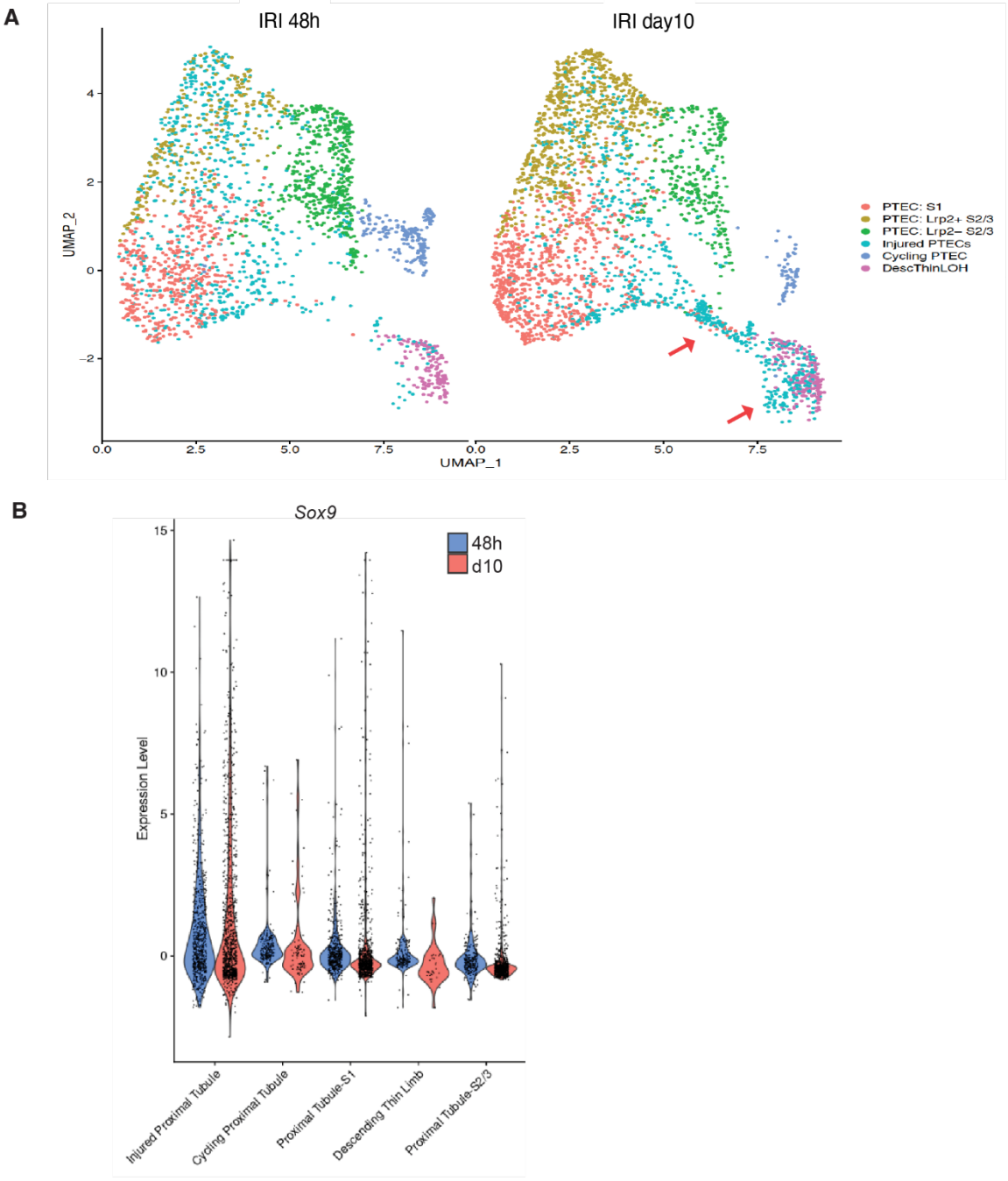

Figure S5. Single cell RNA-seq analysis highlights the emergence of cells with distinct transcriptome in the proximal tubular compartment of acutely injured kidneys.
(A) Time-resolved UMAP projection of the proximal tubular compartment showing emergence of cells with distinct transcriptome at day10 post IRI (red arrows). Note, *Sox9* and *Cdh6* expressing cells contributed to the cluster highlighted by arrows (see also UMAP plots for *Sox9* and *Cdh6* in **Fig. 1**).
(B) Violin plots for *Sox9* expression showing injured proximal tubular epithelial cells followed by cycling proximal tubular epithelial cells, exhibit highest expression, but comparable between 48h and day10 post-injury.
Note, the clusters are arranged from left to right by the scaled average *Sox9* expression.

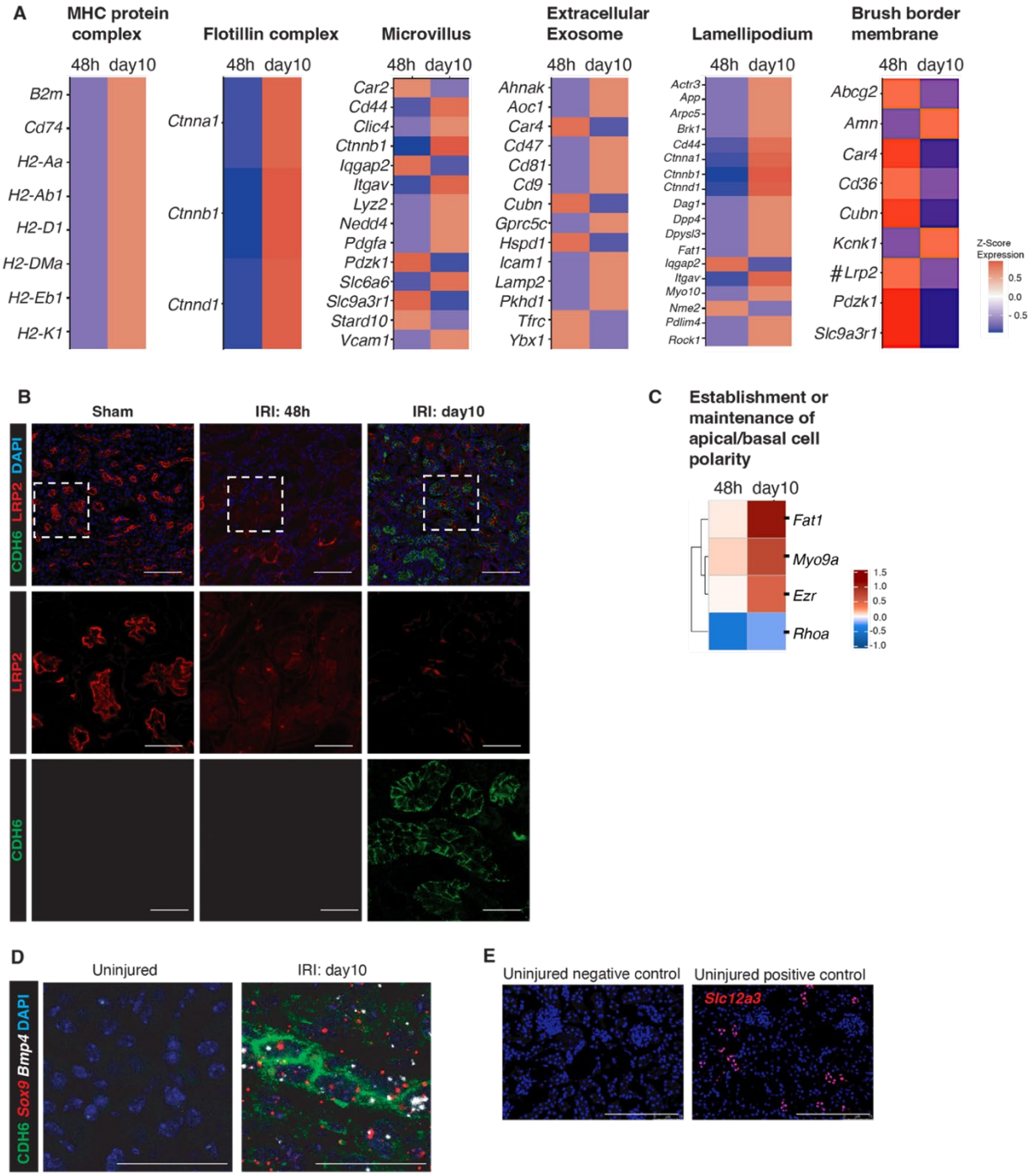

Figure S6. scRNA-seq reveals CDH6^{pos}*Sox9*^{pos} cells are Megalin^{low} and *Bmp4* enriched cell state.
(A) Heatmap of expression of genes driving the enriched GO terms within Sox9$^{on\text{-}on}$ cells versus Sox9^{on} cells (see also Fig. 1).
(B) Co-immunostaining for CDH6 and LRP2 (encodes megalin, an apical brush border protein) showing CDH6^{pos} cells lack megalin. Note, no detectable injury-induced CDH6 expression at 48h after IRI.
(C) Heatmap of expression of genes involved in apicobasolateral polarity that were differentially expressed between Sox9$^{on\text{-}on}$ cells versus Sox9^{on} cells.
(D) RNAscope study involving immunostaining for CDH6 and detection of *Bmp4*, *Sox9* mRNA showing *Bmp4*$^{+}$*Sox9*$^{+}$CDH6^{+} cells, further, validating the scRNA-seq analysis. See **Fig. 1** for *Bmp4* enrichment.
(E) RNAscope study showing additional controls (*Slc12a3* + cells) utilized with (**D**).
n=3 animals/time-point. Scale bars: 100µm.

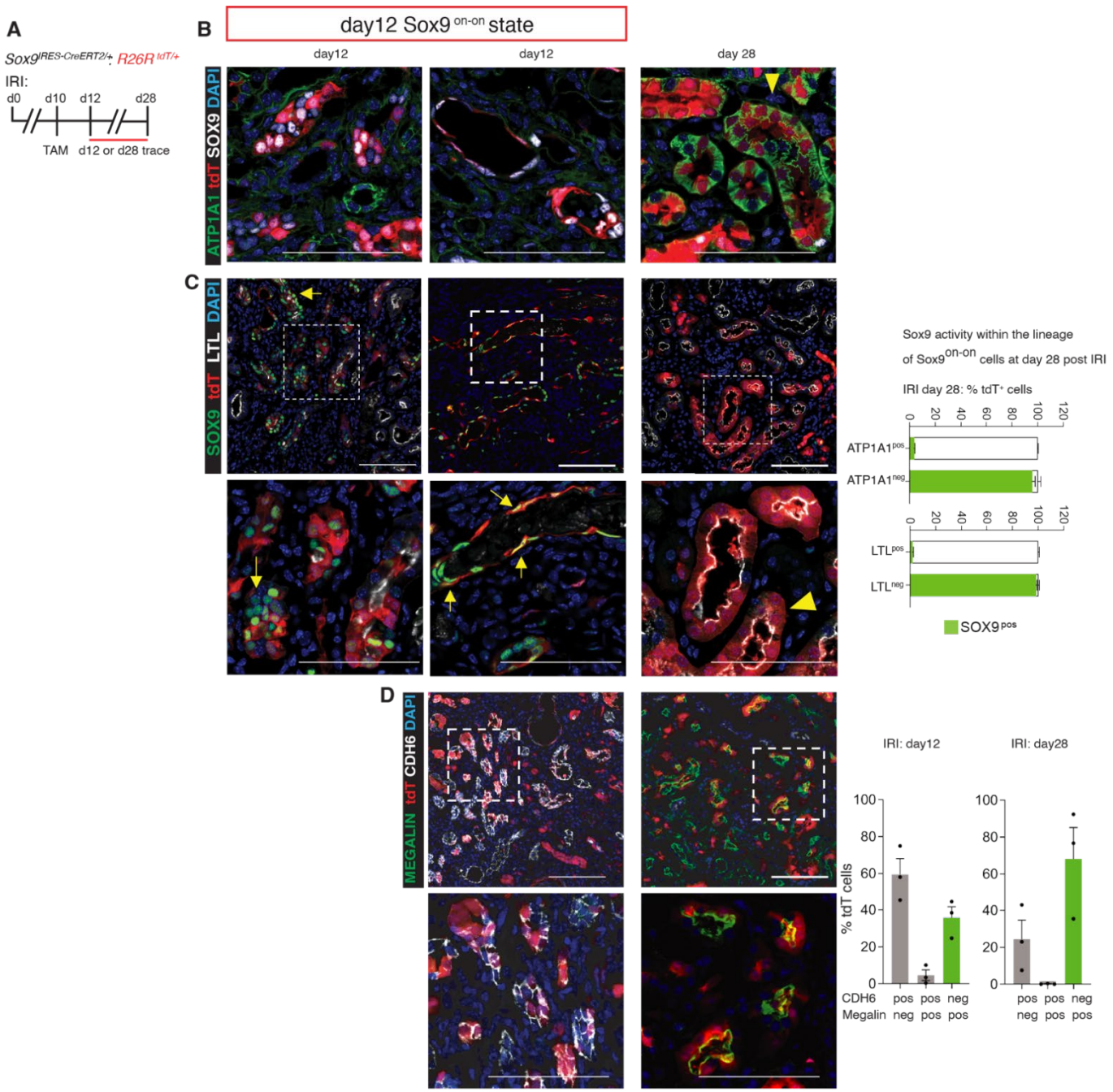

Figure S7. Lineage tracing of Sox9$^{on\text{-}on}$ cells highlight repair capability and continuum of adaptive Sox9/Cdh6 activity during progression of AKI to CKD phase.

(A) Schema of lineage-tracing strategy of Sox9$^{on\text{-}on}$ cells after IRI.

(B, C) Co-immunoanalysis for SOX9 and ATP1A1 **(B)**, LTL **(C)**, respectively, showing Sox9$^{on\text{-}on}$ cells lacked LTL^{+} apical brush border and ATP1A1^{+} basolateral polarity, irrespective of region. Colocalization of SOX9^{+} cells with Sox9-CreERT2-activated tdT fluorescence (tdT^{+} cells) demonstrating fidelity of the reporter for Sox9 in the day12 tissue damaged microenvironment. Arrows showing distinct morphological features of subset of Sox9$^{on\text{-}on}$ cells: grape-like clusters and re-lining of tubules with elongated nuclei akin to fig. **S1G**. At day28 post-IRI, the subset of Sox9$^{on\text{-}on}$ lineage that repaired the epithelia reflected by restored apico-basolateral polarity had silenced SOX9 activity (**B, C,** arrowheads). For total cells counted, see table S2.

(D) Co-immunoanalysis for CDH6 and megalin (encoded by *Lrp2*) showing dynamic Cdh6 activity, in addition to, capability to repair as highlighted by restoration of megalin^{pos} apical polarity and switching off CDH6 expression at day 28. n=3 animals/time-point. All images/time-point obtained from the same tissue section. Scale bars: 100µm.

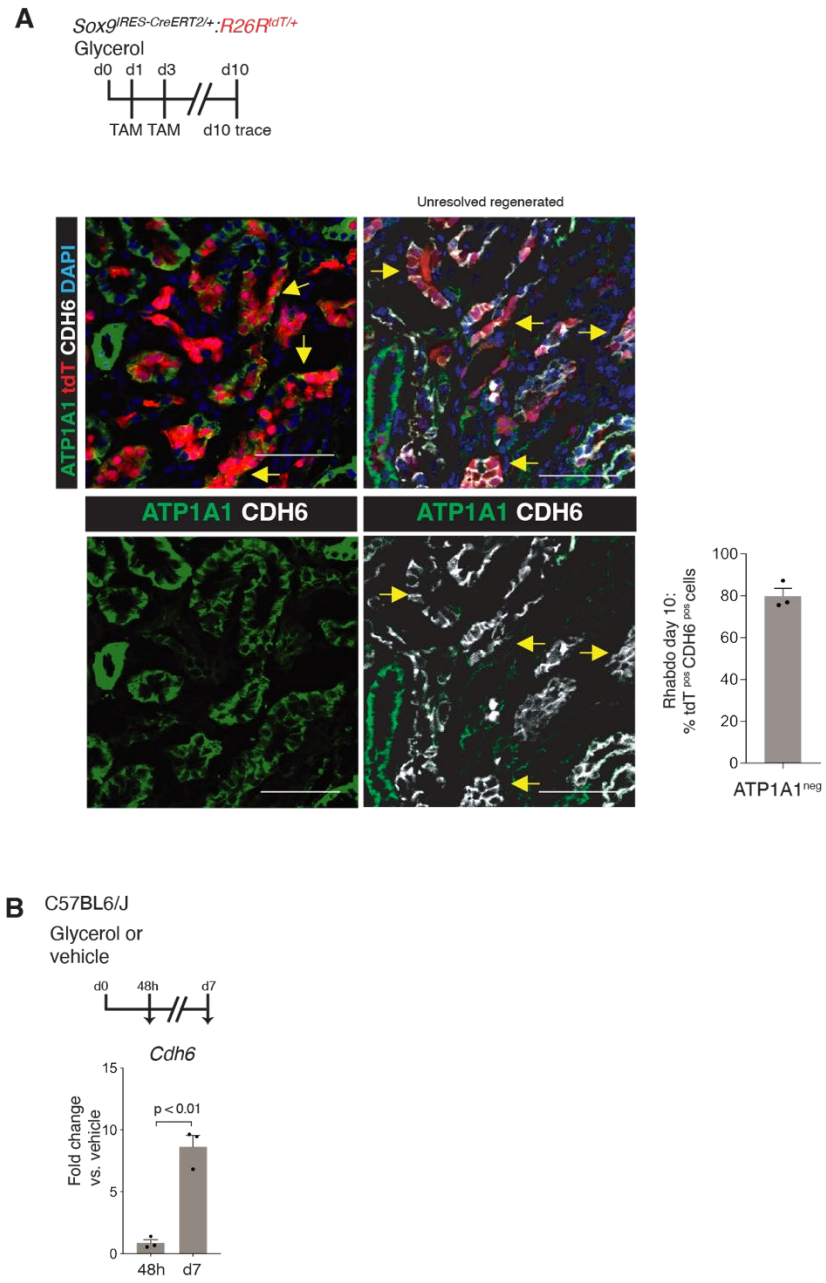

Figure S8. Injury-induced Sox9 lineages display dynamic Sox9/Cdh6 switch after rhabdomyolysis-AKI.

(A) Schema of lineage-tracing cells that activated Sox9 post rhabdo-AKI and co-immunoanalysis showing that at day10 post glycerol injection, CDH6 demarcated Sox9$^{on\text{-}on}$ cell state. Note, restriction of CDH6 expression within Sox9-lineage with unrestored ATP1A1 polarity, whilst the ones that restored basolateral polarity were CDH6^{negative}.
(B) QPCR of kidneys post rhabdo-induced AKI for *Cdh6*. Unpaired Student's t-test. n=3 animals/time-point.
Scale bars: 100µm.

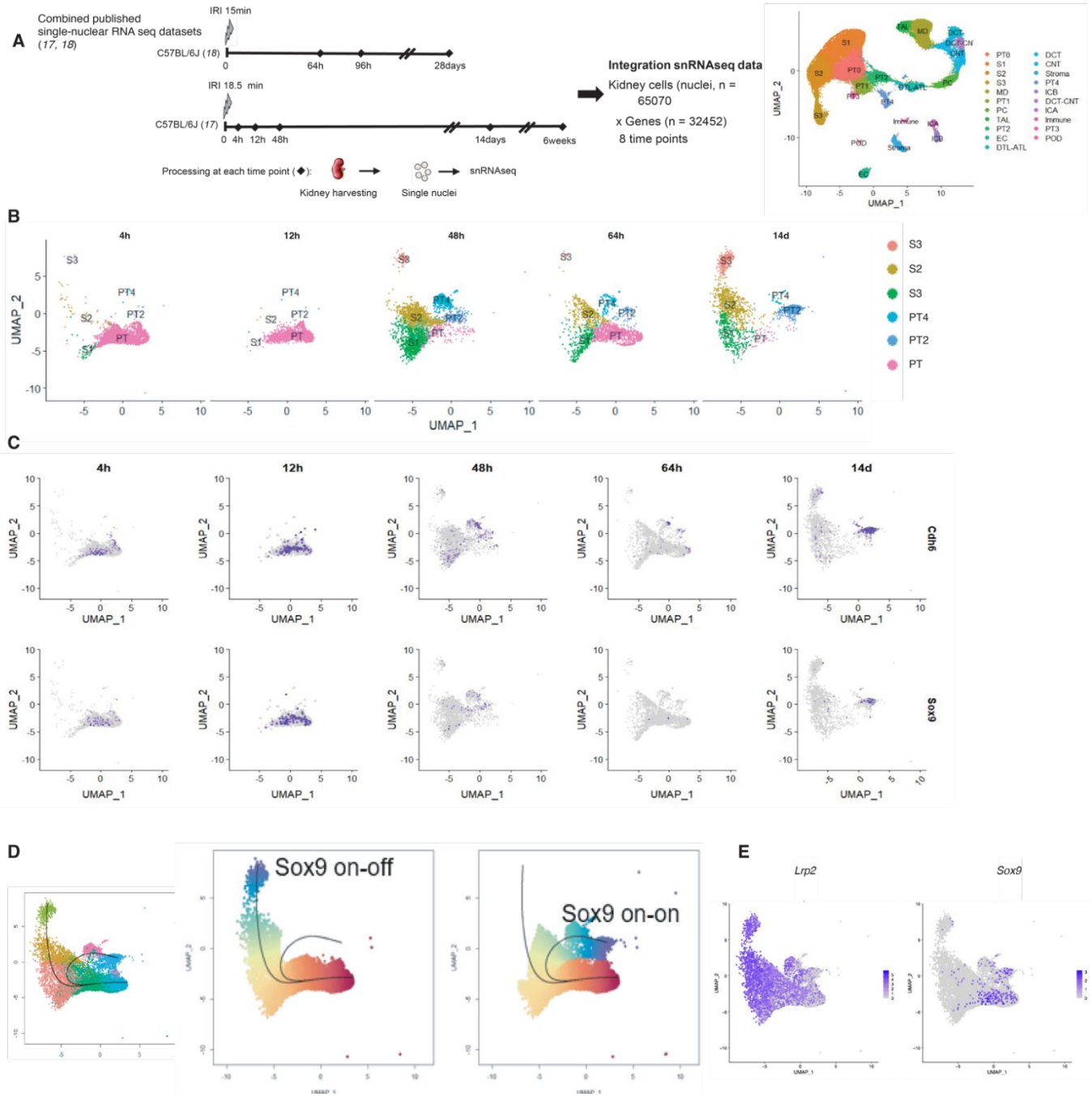

Figure S9. Single-nuclear dynamic Sox9 activity paralleling regenerative state of its lineage after IRI-induced AKI.

(A) Schematic summary of the composition of the integrated snRNAseq dataset. The dataset includes models of transition from AKI to CKD. After IRI, the kidneys are harvested at 4h, 12h, 48h, 64h, 96h, 14d, 28d and 6w and analyzed by single nucleus RNA sequencing. UMAP of the integrated datasets.
PT, Proximal Tubules; DTL-ATL, Descending Thin Limb- Ascending Thin Limb; TAL, Thick Ascending Limb; PC, Principal Cells; ICA, Intercalated Type A cells; ICB, Intercalated type B cells; Pod, Podocytes; EC, Endothelial Cells.
(B) UMAP projection of the proximal tubular compartment resolved over time (at 4h, 12h, 48h, 64h, 14d) showing the presence of clusters in normal (S1, S2, S3) and altered states (PT, PT2, PT4).
(C) Feature plot showing *Cdh6* and *Sox9* expression with time.
(D) Trajectory analysis identifies the two lineages associated with *Sox9*$^{on\text{-}off}$ cells which reacquire a normal phenotype and *Sox9*$^{on\text{-}on}$ cells which persist in an altered state.
(E) Feature plot showing *Lrp2* and *Sox9* expression demonstrating *Lrp2* state of the two distinct Sox9 lineages.

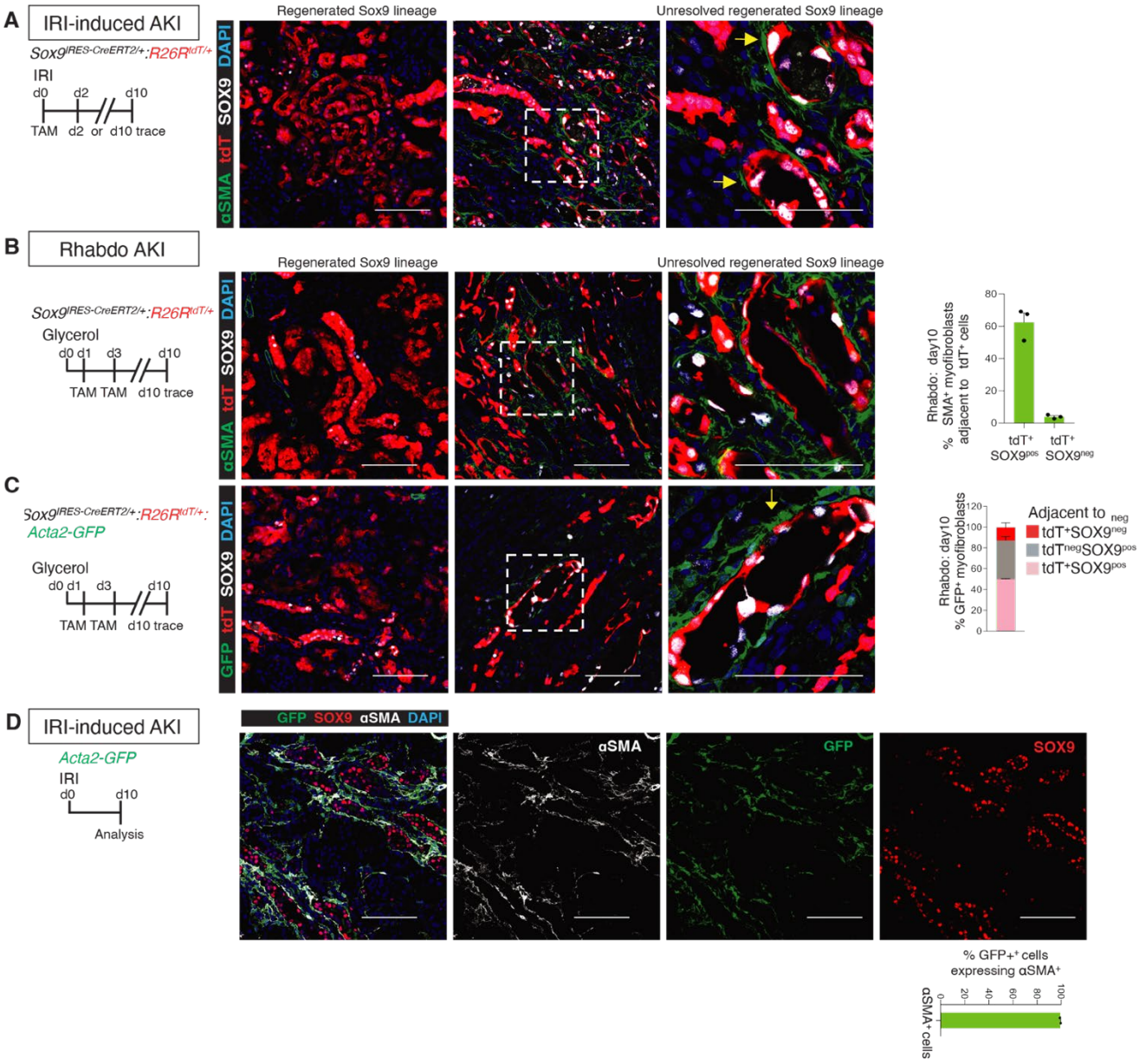

Figure S10. Sox9$^{on\text{-}off}$ cells heal with no scar, but Sox9$^{on\text{-}on}$ cells, display robust, single-cell spatial association with αSMA^{+} myofibroblasts within the same tissue damaged microenvironment after AKI.

(A) Schema of lineage-tracing of IRI-induced Sox9^{+} cells. Co-immunoanalysis showing αSMA^{+} myofibroblasts encased SOX9^{+}tdT^{+} cells (Sox9$^{on\text{-}on}$ cells, arrows), contrasting with the lack of αSMA activity around the Sox9-lineage that successfully restored the epithelia (SOX9^{neg}tdT^{+}; Sox9$^{on\text{-}off}$ cells). The latter feature highlights "regeneration with no scar". Note, αSMA^{+} response paralleled proportion of Sox9$^{on\text{-}on}$ cells.
(B, C) Schema of lineage-tracing of cells that activate Sox9 early after rhabdomyolysis-induced AKI (Rhabdo-AKI) in *Sox9*$^{IRES\text{-}CreERT2/+}$:*R26R*$^{tdT/+}$ (**B**) and *Sox9*$^{IRES\text{-}CreERT2/+}$:*R26R*$^{tdT/+}$:*Acta2*-GFP mice (**C**). Co-immunoanalysis showing αSMA^{+} myofibroblasts adjacent to Sox9$^{on\text{-}on}$ cells, with striking paucity of αSMA^{+} myofibroblasts around the SOX9^{neg}tdT^{+} at 10 days post-IRI (**B**). Co-immunoanalysis for SOX9 showing distinct juxtaposition between GFP^{+} and Sox9$^{on\text{-}on}$ cells at single-cell spatial distance (arrow), whilst no GFP^{+} cells were detected adjacent to SOX9$^{on\text{-}off}$ cells (**C**). For total cells counted, see table S2.
(D) Immunoanalysis for αSMA and SOX9 in kidneys harvested from *Acta2*-GFP animals showing cells with green fluorescent protein (GFP^{+} cells) were αSMA^{+} thus validated the *Acta2*-GFP mice for Acta2 activity. Note, the tight association of most of the αSMA^{+} myofibroblasts with SOX9^{+} cells. Scale bars: 100μm.

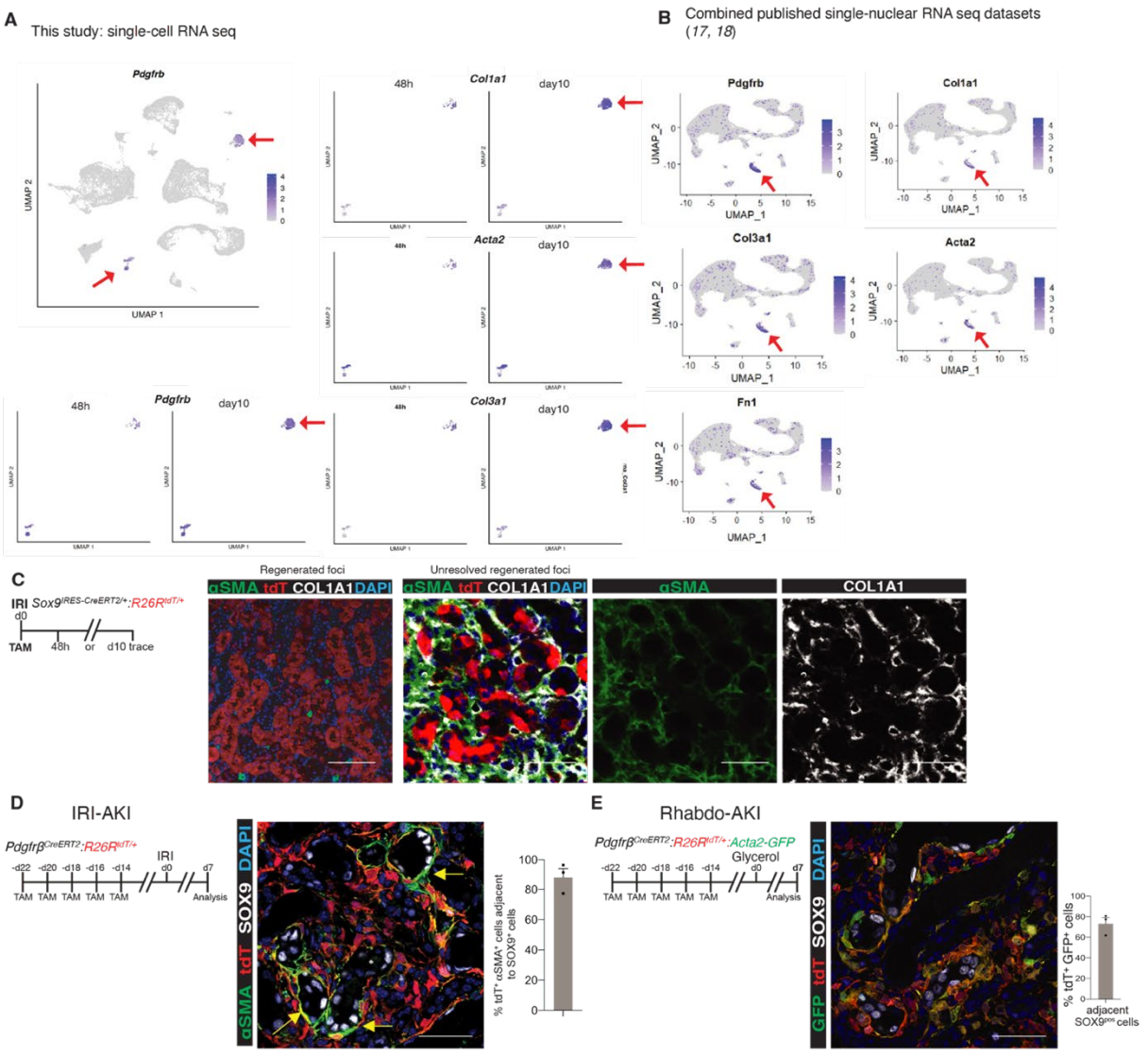

Figure S11. Single-cell sequencing analysis showed no distinct cell clusters of scar-forming cells after IRI-induced AKI.

(A) UMAP representation of *Pdgfrb*$^{+}$ stromal cells and the time-resolved UMAP representation of *Col1a1, Acta2, Col3a1* and *Pdgfrb* expressing cells revealed a distinct increase in the proportion of all three scar-forming cells at day 10 post-IRI. These cells, which activated the fibrotic responses, clustered together (arrows), further corroborating the single-cell datasets for scarring responses.

(B) UMAP representation of *Pdgfrb, Col1a1, Col3a1, Acta2*, and *Fn1* expressing single-nuclear cells in published datasets (*17, 18*) demonstrating all such scar forming cells cluster together (arrows).

(C) Schema of lineage tracing injury-induced Sox9^{+} cells, with co-immunoanalysis for αSMA and COL1A1 showing co-expression of αSMA and COL1A1 within the same cell-type. Note, no detectable COL1A1 or αSMA expressing myofibroblasts in the foci of regenerated epithelia at 2 weeks post-IRI, in contrast, the αSMA^{+}COL1A1^{+} cells encased the regenerating Sox9-lineage. Co-localization of αSMA and COL1A1 response validated the above single-cell and nuclear sequencing datasets.

(D) Schema of labeling resident Pdgfrb^{+} cells. At day7 post IRI, co-immunoanalysis showing subset of interstitial tdT^{+} cells that resided at single-cell spatial distance to SOX9$^{on\text{-}on}$ cells, formed αSMA^{+} myofibroblasts (arrowheads). Note, the exclusive spatial association of αSMA^{+} and SOX9^{+} foci (arrows).

(E) Schema of labeling resident Pdgfrb^{+} cell-type in *Pdgfrb*$^{CreERT2/+}$*:R26R*$^{tdT/+}$*:Acta2*-GFP mice . Co-immunoanalysis for SOX9 showing nearly all the GFP^{+} cells co-localized with tdT^{+} cells (tdT^{+}GFP^{+} cells), with vast majority of such tdT^{+}GFP^{+} myofibroblasts next to SOX9^{+} cells (arrows), thus highlighting the tight association in post-rhabdo AKI, too. For total cells counted, see table S2. n=3 animals. Mean ± SEM. Scale bars: 100μm.

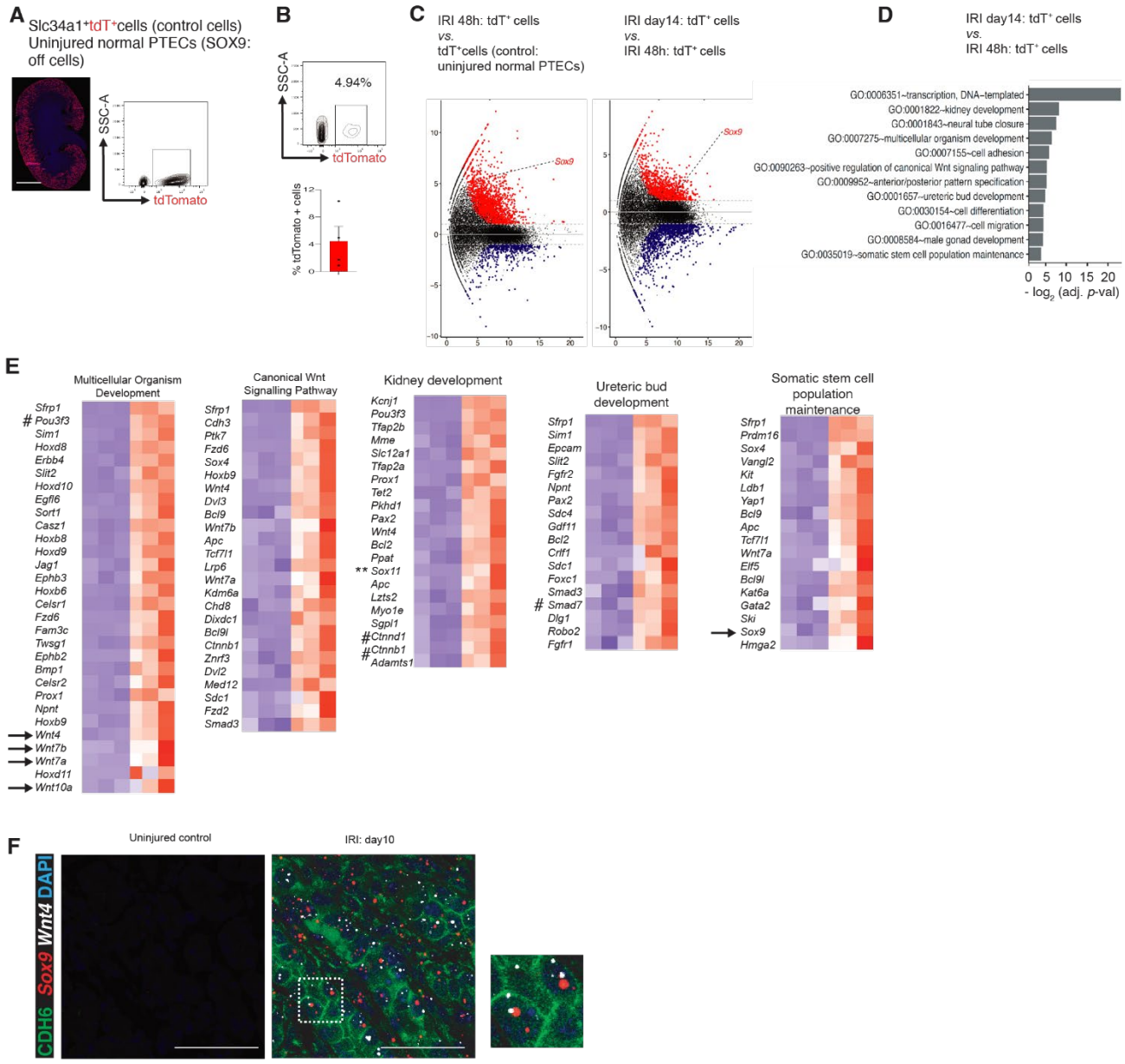

Figure S12. Temporal Sox9 cell-type specific transcriptomic profiling reveals Sox9$^{on\text{-}on}$ cells form *Wnt* enriched cells with time.

(A) Whole scanned kidneys showing *Slc34a1*$^{+}$ labeled normal proximal tubular (PT) cells and representative FACS plots showing purified control tdT^{+} population from uninjured *Slc34a1*$^{CreERT2/+}$:*R26R*$^{tdT/+}$ animals. Scale bar: 1000µm.

(B) Representative FACS plots showing purified tdT^{+} cells at IRI d14: Sox9^{+}tdT^{+}. See **Fig. 2C** for labeling schema of purified tdT^{+} cells.

(C) Volcano plots highlighting significant Sox9 enrichment.

(D) GO analysis showing significantly enriched biological processes (BP) amongst the 15 topmost BP within IRI d14: Sox9^{+}tdT^{+} vs. d2: Sox9^{+}tdT^{+} cells.

(E) Heatmap of expression profiles of genes driving the enriched GO enriched terms. Arrows highlighting enrichment of *Wnts*: candidate secretory ligands for adjacent myofibroblast formation (see also **Fig. 2F**). # highlighting genes within the enriched GO terms of scRNA seq datasets, see **Fig. 1.** ** highlights *Sox11*, see also **Fig. 2E, H.**

(F) RNAscope study showing CDH6^{+}*Sox9*$^{+}$*Wnt4*$^{+}$ cells. See also **Fig. 2F to I** for cross validation and to determine the identity of Sox9 expressing cells that mounted the identified *Wnt* response at the single-cell level. Square inset highlights the foci depicted in the magnified panel (right). n = 3-5 animals/time-point. Scale bars:100µm.

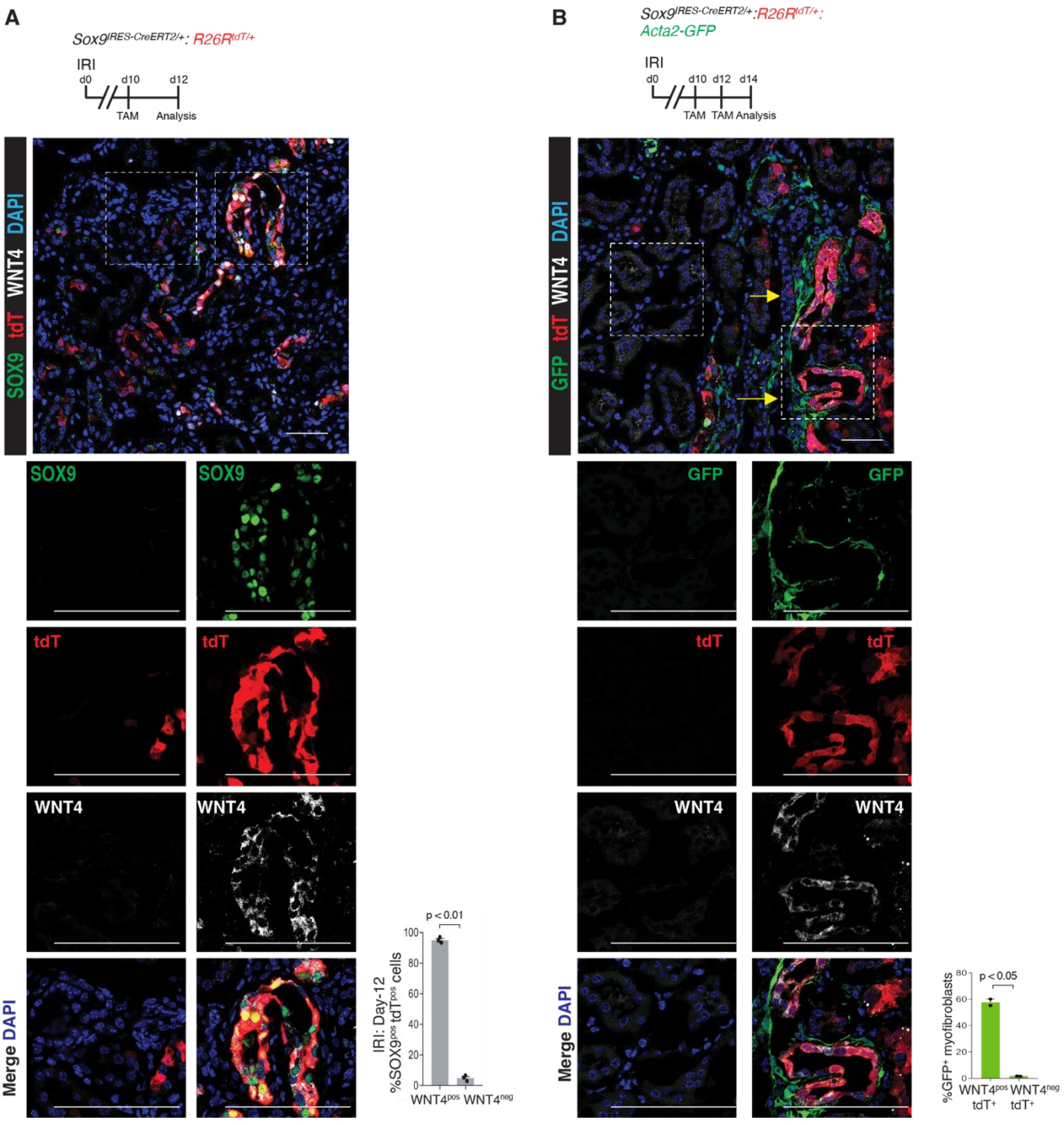

Figure S13. Sox9$^{on\text{-}on}$ cells maintain active Wnt4 activity during progression of AKI to CKD.
(A,B) Schema for demarcation of Sox9$^{on\text{-}on}$ cells in *Sox9$^{IRES\text{-}CreERT2/+}$:R26R$^{tdT/+}$* and *Sox9$^{IRES\text{-}CreERT2/+}$:R26R$^{tdT/+}$:Acta2-*GFP animals, respectively, during AKI to CKD progression. Co-immunoanalysis for SOX9 and WNT4 showing co-localization of WNT4 expression with SOX9^{+}tdT^{+} cells (Sox9$^{on\text{-}on}$ cells, **A**). Note, such cells displayed intimate, near exclusive association with GFP^{+} myofibroblasts (**B**, arrows).
p-value via unpaired Student' s t-test. Mean ± SEM. For total cells counted, see table S2. Scale bars: 100μm.

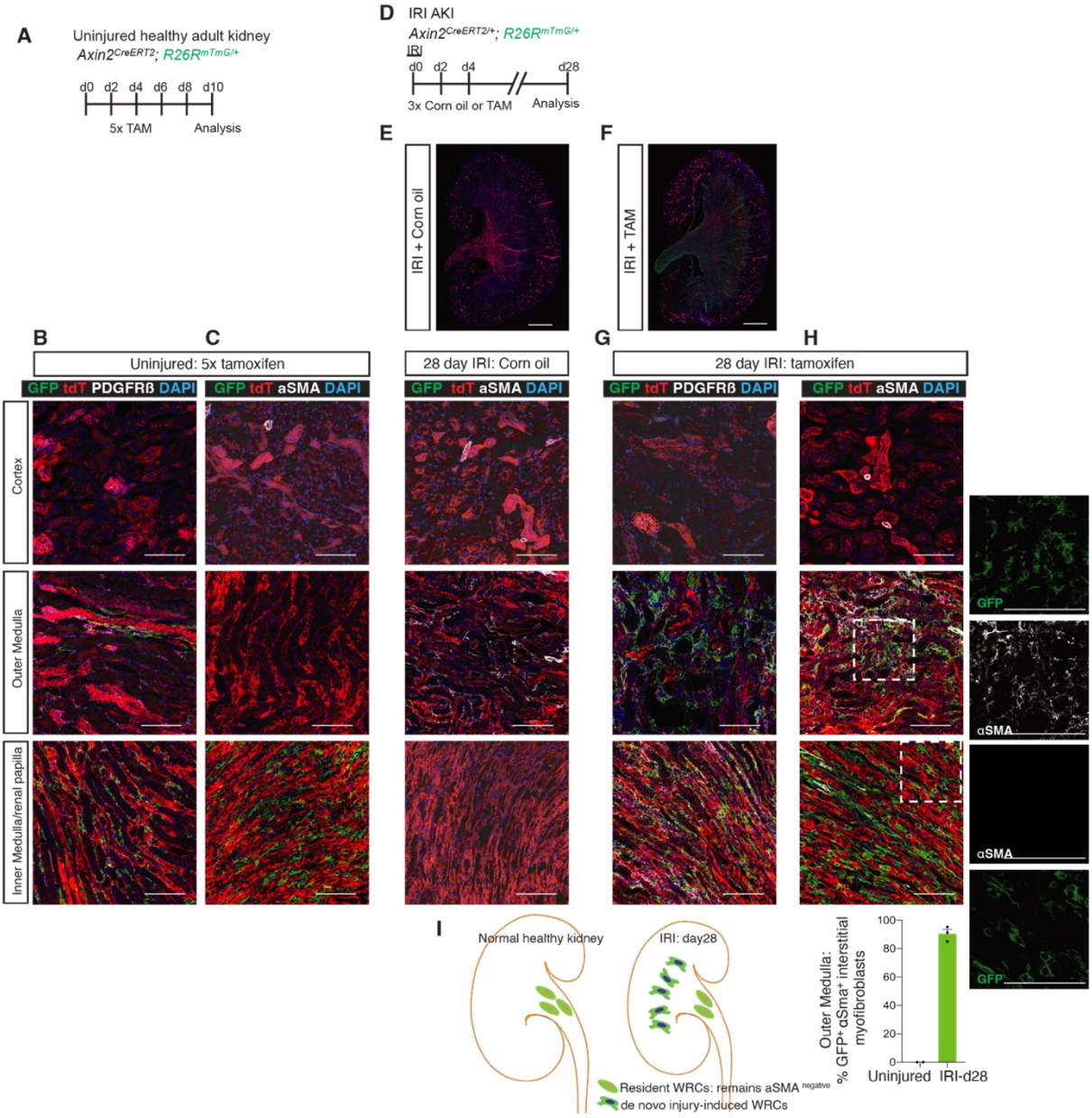

Figure S14. Outer medullary αSMA^{pos}Pdgfrb^{pos} myofibroblasts are IRI-induced Wnt responsive cells.
(A,B) Schema for labeling *Axin2* ^{pos} cells to identify Wnt-responsive cells (WRCs) in adult, normal uninjured kidneys (**A**) and co-immunostaining showing resident PDGFRb^{pos} cells predominantly within the inner medulla/renal papilla express mGFP (**B,** membrane-bound form of GFP, mGFP^{pos}). Note, no WRCs in the adult nephron epithelia. n=2 mice.
(C) Co-immunostaining showing αSMA^{neg} status of resident WRCs (mGFP^{pos} cells).
(D) Schema of only corn oil or tamoxifen administration post-IRI.
(E) Whole kidney image from corn oil injected animals and co-immunostaining showing no GFP^{pos} cells, thus, confirmed tamoxifen-dependence.
(F-I) Whole kidney image from tamoxifen injected animals and co-immunostaining showing injury-induced mGFP^{pos}PDGFRb^{pos} cells in the outer medullary region activated αSMA. Note, the resident WRCs of the inner medulla/papilla region remained αSMA^{neg} and the nephron tubular epithelial compartment did not display injury-induced mGFP^{pos} cells. αSMA^{pos} myofibroblasts of the outer medullary region represent de novo injury induced WRCs (model, **I**).
Dashed square insets (**H**) highlight the foci represented in the magnified panel (right).
All images are representative images. Quantification: 1476 mGFP^{+} cells counted, n=3 mice.
Scale bars: whole scanned image (**E, F**) 1000µm, others: 100µm.

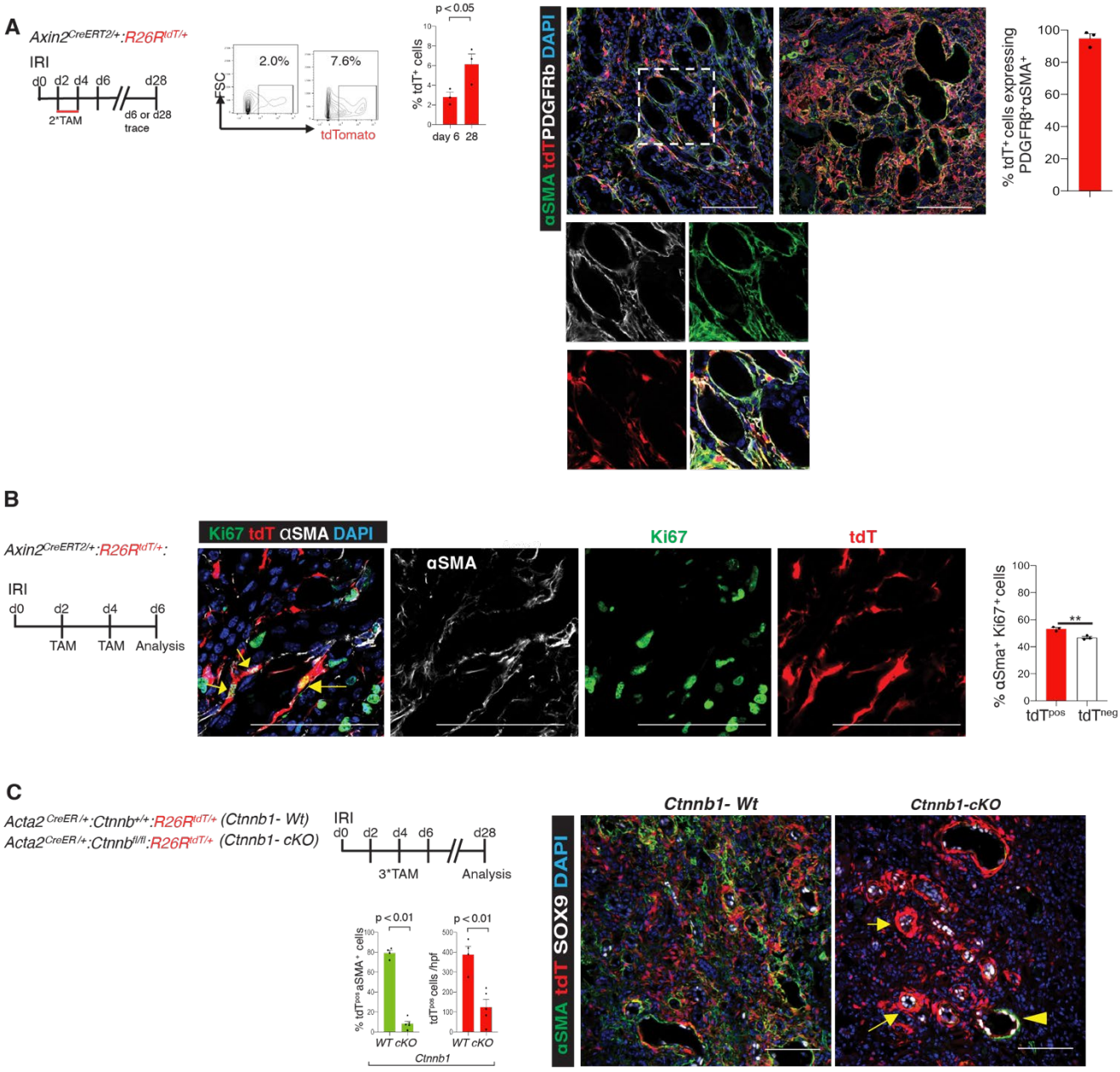

Figure S15. *Axin2*^{pos} lineage contributes to the bulk of fibrotic scar tissue with *β-catenin* essential for maintenance of αSMA activity during progression of AKI to CKD.

(A) Schema of lineage tracing of cells that activated *Axin2* early after IRI, and FACS-based quantification (representative images) showing tdT$^+$ cells as PDGFRβ$^+$ αSMA$^+$ myofibroblasts whose lineage contributed to the bulk of scar tissue by day28 (n=3 animals/time-point).

(B) Schema of labeling cells that activated *Axin2* early after IRI, with co-immunoanalysis showing Ki67$^+$tdT$^+$αSMA$^+$ myofibroblasts (arrows). Quantification shows the proportion of tdT$^+$αSMA$^+$ cells expressing Ki67. αSMA$^+$Ki67$^+$ cells counted, 527; n=3 mice.

(C) Schema of *Ctnnb1* removal from early *Acta2* ^{pos} myofibroblasts, with blinded co-immunoanalysis showing *Ctnnb1* deficient tdT$^+$ myofibroblasts displayed significantly reduced expansion and αSMA activity (arrows), despite single-cell spatial distance with SOX9^{pos} cells. Note, the non-recombined (tdT^{neg}) cells maintained strong αSMA activity (arrowhead). (wild-type controls, n = 4 and *Ctnnb1* cKO, n = 5, blinded analysis).

All images are representative images. Mean ± SEM. *p < 0.05, unpaired Student's t-test.

For total cells counted, see table S2. Scale bars: 100μm.

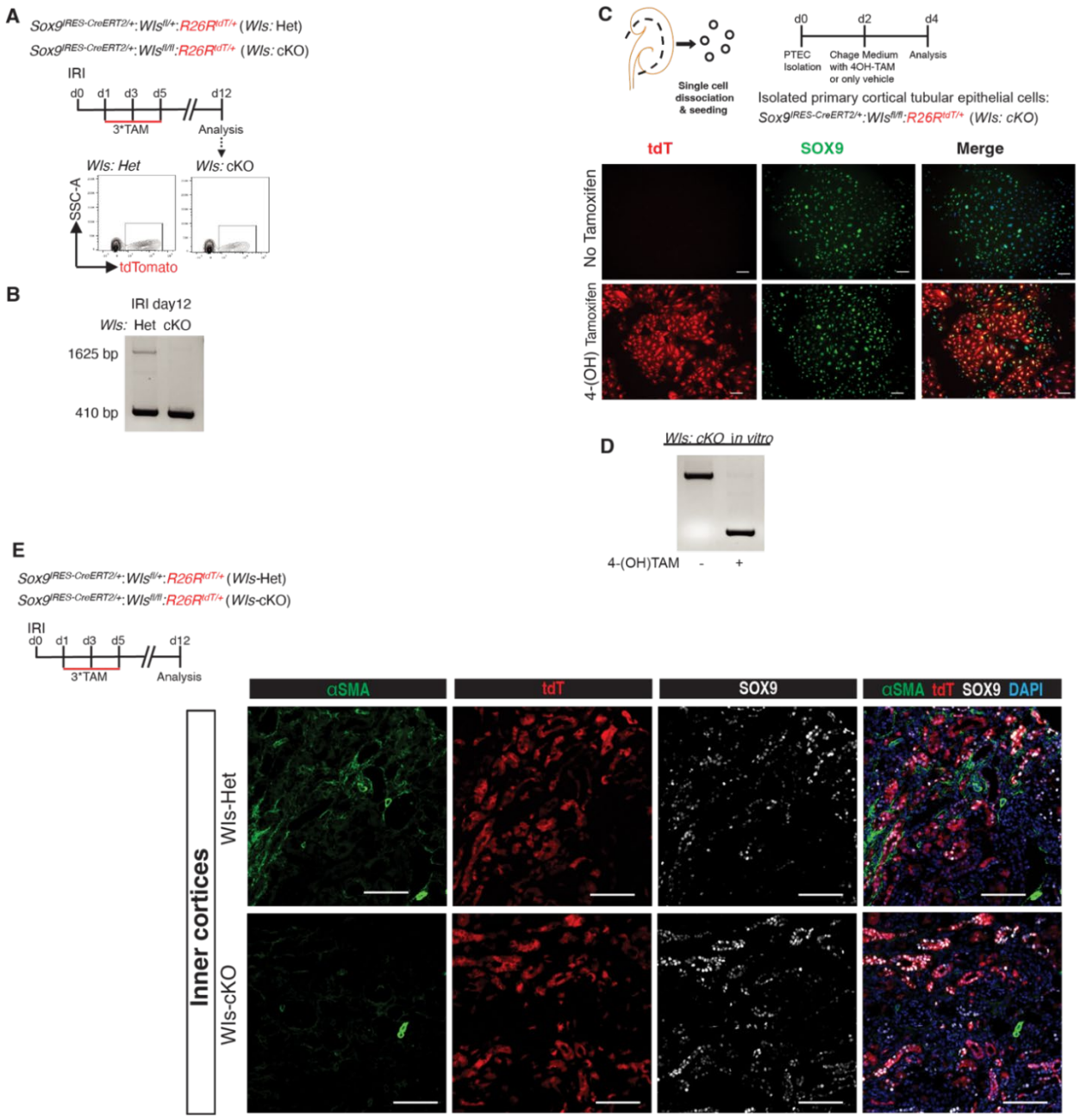

Figure S16. Validation of *Wntless* removal strategy from Sox9$^{on\text{-}on}$ cells.
(A) Experimental outline of tamoxifen regime to delete *Wntless* (*Wls*) from Sox9$^{on\text{-}on}$ cells post-IRI. FACS plot of purified tdT^{+} cells from control and Sox9-cell-type specific *Wls* cKO animals.
(B) PCR analysis on DNA from sorted cells confirmed Cre-mediated excision of *Wls* floxed allele from such cells.
(C) Schema of isolated primary PTECs from the outer renal cortices of *Sox9$^{IRES\text{-}CreERT2/+}$:Wls$^{fl/fl}$:R26R$^{tdT/+}$* animals and co-immunoanalysis for SOX9. Note, exposure to 4-hydroxytamoxifen (4-OHTam) but not vehicle led to Cre-mediated recombination highlighted by tdT^{pos} cells, the latter co-expressing SOX9, further confirming tamoxifen dependence and fidelity of the system.
(D) PCR analysis on DNA from such cells confirmed tamoxifen-dependent, Cre-mediated excision of the *Wls* floxed allele within such cells.
(E) Schema of *Wntless* (*Wls*) removal from Sox9$^{on\text{-}on}$ cells and representative image of the inner cortex showing striking reduction in αSMA^{pos} myofibroblasts (n=5 animals/group). Note, no difference in SOX9$^{on\text{-}on}$ cells between the two groups. See also **Fig. 3** for representative image from the outer medullary region and quantification.
All images are representative images. Scale bars: 100μm.

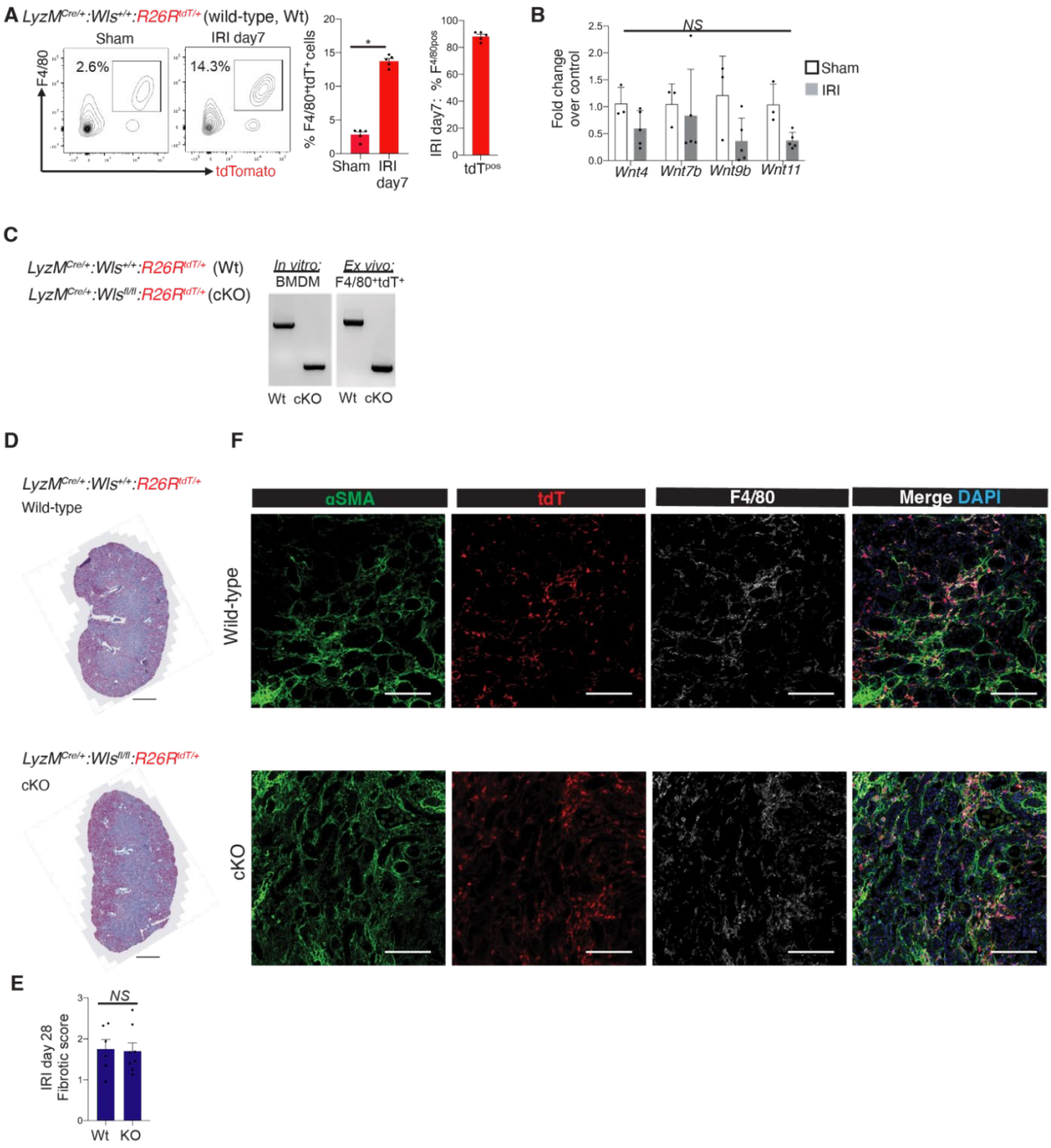

Figure S17. *Wntless* removal within LyzCre-derived immune cells does not impact post-IRI induced fibrosis.
(A) *LyzM*$^{Cre/+}$:*R26R*$^{tdT/+}$ animals were subjected to sham or renal IRI surgery. FACS plot and quantification showing significant increase in F4/80^{+} macrophage population with F4/80^{+} macrophages expressing tdT at day7 post IRI.
(B) qPCR analysis of *Wnt4*, *Wnt7b*, *Wnt9b*, and *Wnt11* in FACS-purified F4/80^{+}tdT^{+} cells demonstrate no significant upregulation of Wnt ligands under scrutiny, post day7 IRI compared to controls.
(C) Bone-marrow derived macrophages (BMDM) generated from Wt and cKO and FACS-purified tdT^{+}F4/80^{+} cells from post-IRI day 7 kidneys confirmed Cre-mediated excision of *Wntless* floxed allele, thus validating LyzMCre-derived cells-specific *Wntless* knock-out (*LyzM*$^{Cre/+}$:*Wls*$^{fl/fl}$:*R26R*$^{tdT/+}$) animals.
(D, E) Representative images of Trichrome-stained kidney sections (**D**) and interstitial fibrosis score (**E**). Unpaired, 2-sided, Student's t-test. Mean ± SEM.
(F) Co-immunostaining for F4/80 and aSMA^{+} in day 28 post-IRI kidneys harvested from LyzMCre-derived immune cells-specific *Wntless (Wls)* knock-out mice compared with control animals with intact Wntless secretory apparatus showed no effect on fibrosis. All images are representative images. Scale bars: whole scanned image (**D**),1000μm; other: 100μm.

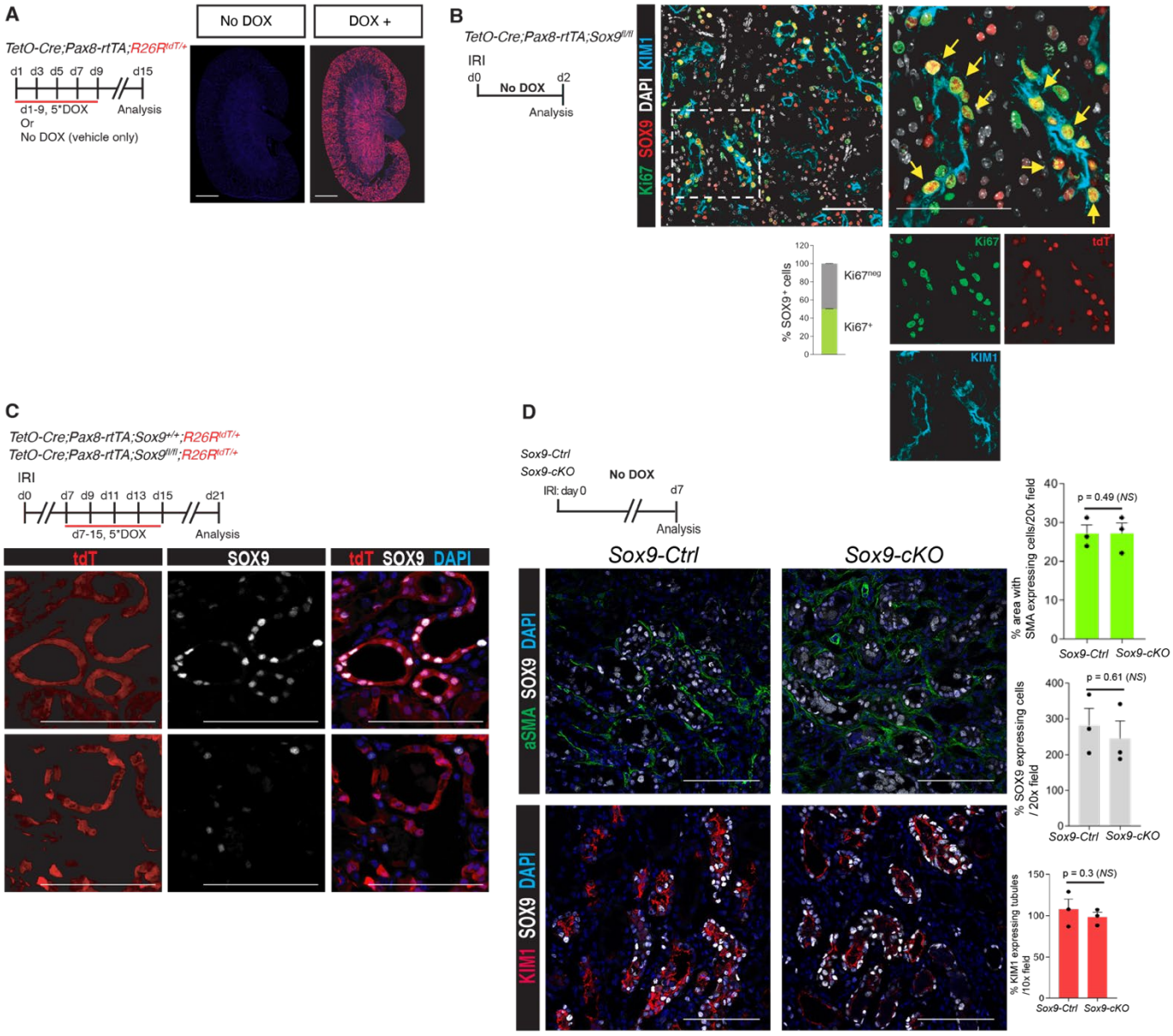

Figure S18. Validation of doxycycline-dependent removal of Sox9$^{on\text{-}on}$ activity during progression of AKI to CKD.

(A) Schema of doxycycline (DOX) regime administered to normal, uninjured, adult animals and whole scanned representative images of kidneys harvested from such animals showing extensive doxycycline dependent recombination in the nephron epithelia (DOX+), in contrast to the only vehicle exposed animals (No DOX) (n=2 animals/group).

(B) Co-immunoanalysis for SOX9, KIM1, and Ki67 in the kidneys harvested from Sox9-cKO animals not exposed to DOX (no DOX) demonstrating preserved early SOX9^{pos}Ki67^{pos} based repair responses (arrows) confirmed doxycycline dependence post-IRI and ruled out IRI-induced spontaneous Cre activation post-IRI. Quantification: % SOX9^{+}Ki67^{+} cells 48h post-IRI (n = 1933 cells counted, n=2 animals).

(C) Schema of DOX regime administered a week post IRI-induced AKI to remove Sox9$^{on\text{-}on}$ activity during transition of AKI to CKD. Co-immunoanalysis for SOX9 showing co-localization of Sox9$^{on\text{-}on}$ cells with tdT^{+} cells in controls, with successful removal of Sox9$^{on\text{-}on}$ activity in the majority of the tdT^{+} cells in Sox9-cKO animals.

(D) Co-immunostaining for αSMA (upper panel) and KIM1 (lower panel) with SOX9 showing similar extent of αSMA and KIM1 expression in Sox9-Ctrl vs. Sox9-cKO at day7 after injury, prior to initiation of Doxycycline. Note, intimate association between SOX9$^{on\text{-}on}$ cells and αSMA^{pos} myofibroblasts. Quantification n=3 animals/group, blinded analysis, unpaired, 2-sided, Student's t-test. All images are representative images. Mean ± SEM. Scale bars: Whole scanned image (**A**) 1000μm, other: 100μm.

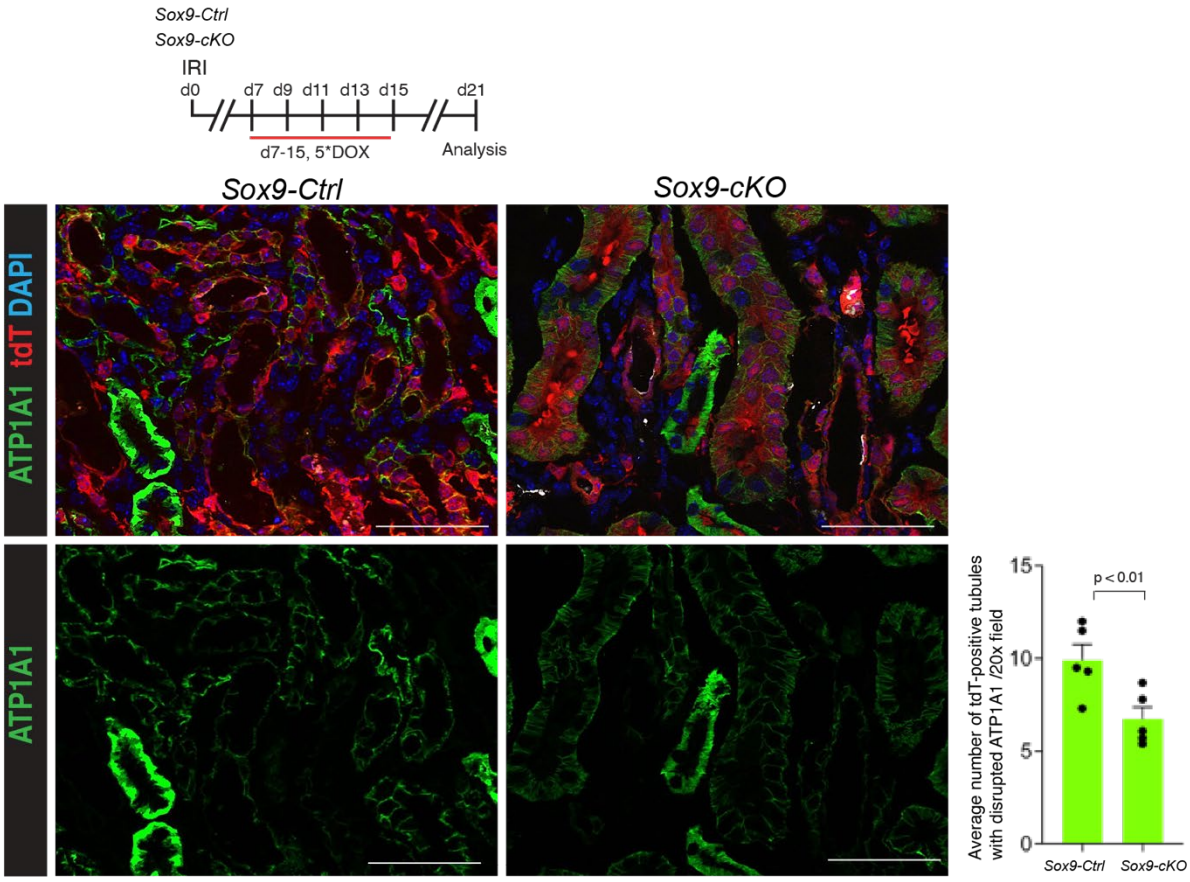

Figure S19. Genetic fate mapping of Sox9^{on-on} deficient cells shows significant reduction in the tubules with disrupted NaKATPase based basolateral polarity.
Co-immunoanalysis for ATP1A1 (NaKATPase). tdT^{pos} showing tubules that underwent recombination in *Sox9-Ctrl* and *Sox9-cKO* animals.
(n = 5 animals/group, blinded analysis, unpaired Student's t-test).
All images are representative images. Mean ± SEM. Scale bars: 100µm.

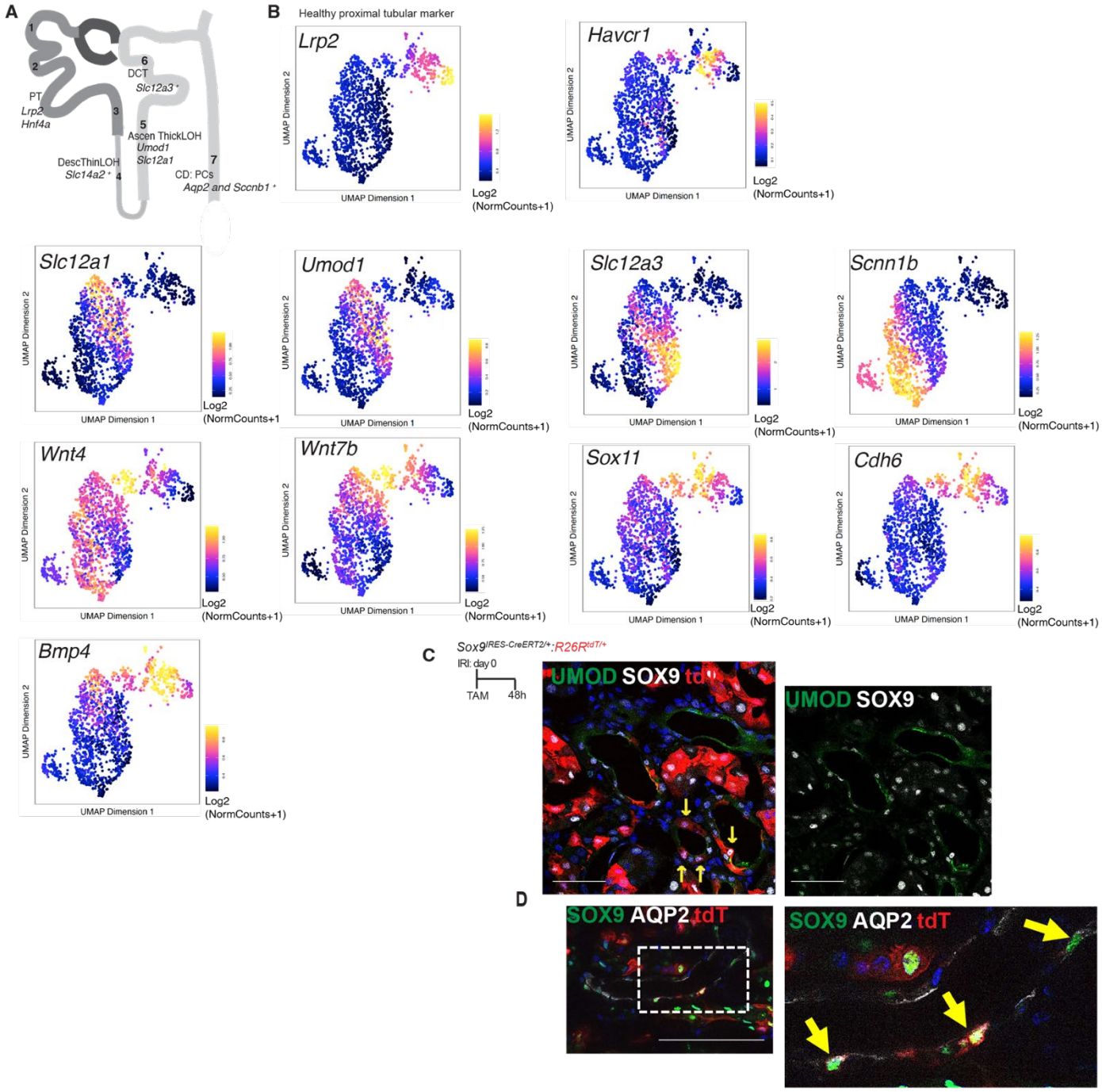

Figure S20. Sox9-lineage specific single-nuclei ATAC analysis demonstrating distinct epithelial type-specific chromatin accessibility profile and validation of cell-type specific activation of Sox9 in other nephron epithelia compartment.

(A) Illustration of nephron showing nephron tubular epithelia and its cell-type specific markers.

(B) UMAP representation of relative chromatin accessibility profile via motifmatrix analysis of cell-type specific genes including *Havcr1*, a proximal tubule injury marker, *Wnt4*, *Wnt7b*, *Bmp4*, *Sox11*, *Cdh6* in line with the single-cell gene expression analysis of day10 *Sox9* vs. 48h *Sox9* (see Fig. 1).

(C) Co-immunostaining for UMOD confirming SOX9 activation in epithelial cells of the thick ascending limb of loop of Henle at 48h post-injury.

(D) Co-immunostaining for AQP2 confirming SOX9 activation in epithelial cells of the collecting duct at 48h post-injury. This SOX9 activation is consistent with single-cell RNA-seq findings (see dot plot **Fig. 1B**). n=2 animals. Scale bars: 100µm.

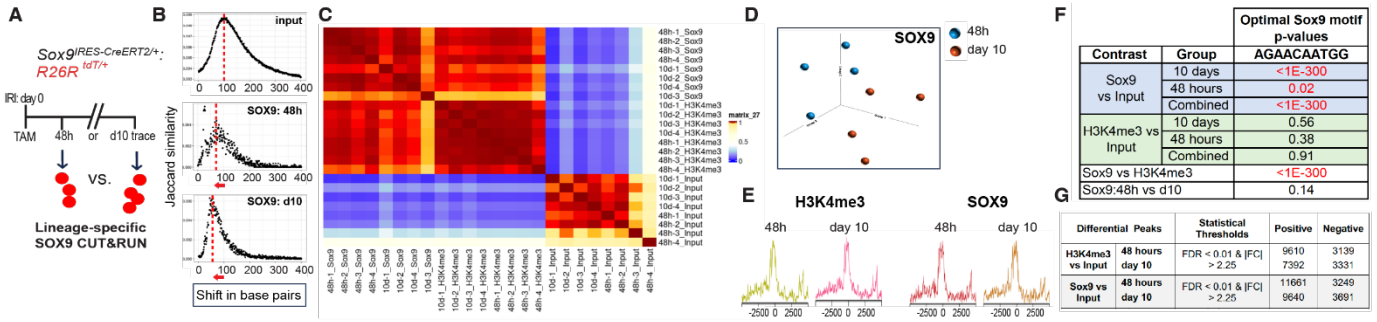

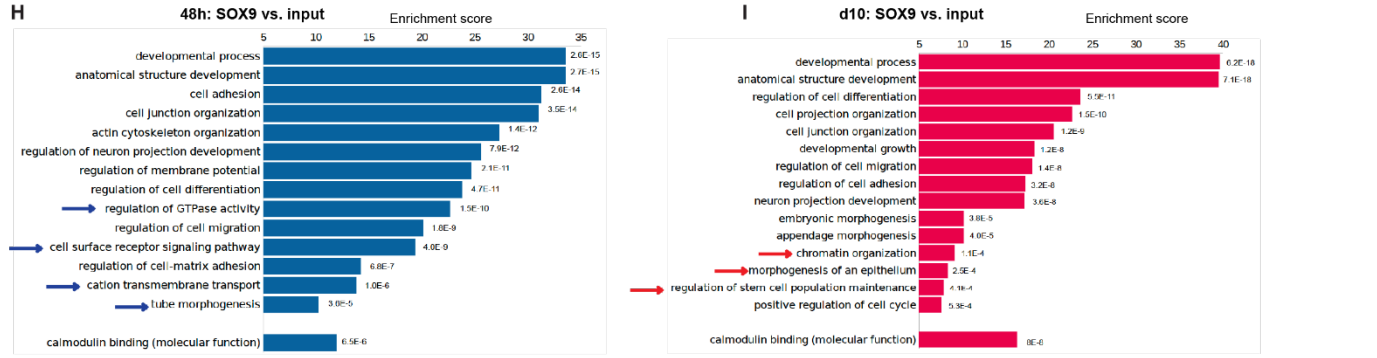

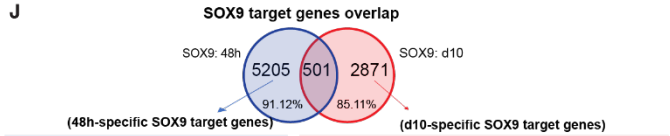

KEGG Pathway term	p-value
Rap1 signaling pathway	4.60E-14
Focal adhesion	2.60E-11
Pathways in cancer	4.90E-11
Calcium signaling pathway	9.70E-09
EGFR tyrosine kinase inhibitor resistance	1.80E-08
Ras signaling pathway	3.00E-08
Axon guidance	1.50E-07
Regulation of actin cytoskeleton	1.50E-06
Tight junction	5.90E-06
ErbB signaling pathway	1.30E-05

KEGG Pathway term	p-value
Metabolic pathways	8.90E-06
Signaling pathways regulating pluripotency of stem cells	3.10E-05
Phosphatidylinositol signaling system	4.10E-05
Pathways in cancer	1.40E-03
Axon guidance	3.00E-03
Regulation of actin cytoskeleton	1.10E-02
Bacterial invasion of epithelial cells	1.50E-02
Wnt signaling pathway	1.70E-02

GO term	p-value
nervous system development	6.30E-19
intracellular signal transduction	1.10E-17
cell adhesion	3.70E-17
cell migration	6.10E-16
ion transport	6.10E-14
multicellular organism development	4.30E-13
actin cytoskeleton organization	1.10E-12
cell-cell adhesion	5.00E-12
cell differentiation	5.70E-12
activation of GTPase activity	3.60E-11
cell proliferation	2.20E-07
in utero embryonic development	3.70E-08
sodium ion transmembrane transport	1.40E-08
Ras protein signal transduction	2.70E-07
cellular calcium ion homeostasis	1.20E-06

GO term	p-value
multicellular organism development	1.20E-09
positive regulation of transcription from RNA polymerase II promoter	8.50E-09
neural crest cell migration	3.00E-06
cellular response to DNA damage stimulus	2.50E-05
cell cycle	3.60E-05
chromatin organization	1.20E-04
cell differentiation	1.20E-04
regulation of double-strand break repair	1.40E-04
cell proliferation	1.50E-04
heart development	3.10E-04
positive regulation of epithelial cell proliferation	9.50E-04
system development	1.20E-03
Wnt signaling pathway	1.70E-03
ureteric bud development	5.10E-03

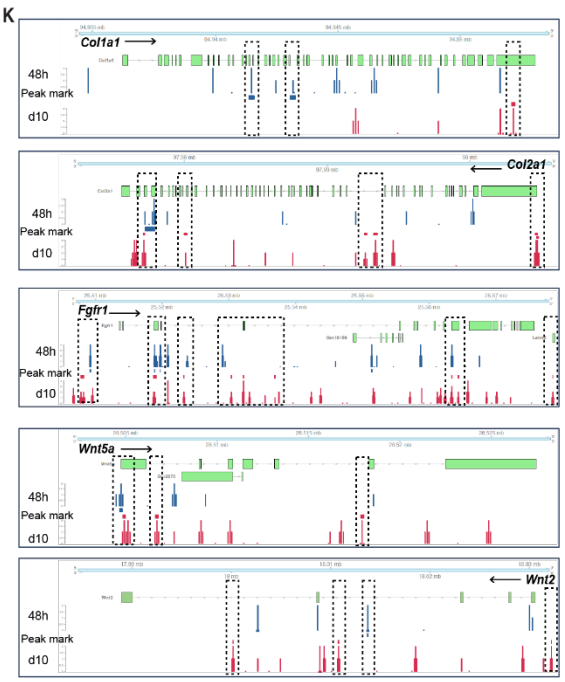

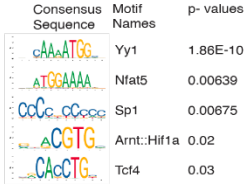

Figure S21. Time-resolved, lineage-specific SOX9 genomic occupancy assay highlights sustained SOX9 activity as an attempt to regenerate its lineage via reprogramming to a progenitor-like cell state.
(A) Schema illustrating the workflow for time-resolved SOX9 CUT&RUN genomic occupancy assay to ascertain the logic for $Sox9^{on\text{-}on}$ activity per se in its lineage. H3K4me3 was used as internal control.
(B) Jaccard similarity index plots showing the expected average DNA fragments obtained in the CUT&RUN and input sequencing, respectively. Note, the shift in base pairs consistent for a transcription factor (red arrows, CUT&RUN vs. input sequencing).
(C) Heatmap showing the pairwise Pearson correlation coefficients between the different datasets generated in each sample.
(D) UMAP embedding showing distinct time-resolved clustering of SOX9 genomic occupancy in its lineage.
(E) Signals of H3K4me3 and SOX9 peaks plotted relative to the transcription start sites.
(F) SOX9 motif in CUT&RUN datasets was significantly enriched indicating a high specificity of the datasets and supporting direct SOX9 target interactions. Note, significant enrichment of the optimal SOX9 binding motif in the SOX9 antibody group compared with their input, including significant enrichment of the motif between CUT&RUN: SOX9 and H3K4me3.
(G) Numbers of positively and negatively enriched differential peaks found between samples of SOX9 and H3K4me3 antibodies and their input.
(H, I) Enriched GO terms of differentially expressed genes in CUT&RUN SOX9 vs. input analysis at 48 hours (**H)** and 10 days **(I)**, after removal of redundant GO terms and GO terms linked with biochemical pathways. Arrows highlighting time-specific, highly enriched GO terms.
(J) Venn diagram depicting significantly enriched time-specific, distinct target genes identified in **(G)** and top significant pathways via KEGG analysis and GO terms of such genes.
(K) Genome browser tracks showing CUT&RUN signals generated with SOX9 antibody at the genomic region of the gene *Col1a1* (48h-specific target gene), *Col2a1* (d10-specific target gene), *Fgfr1* (d10-specific target gene) and reveal direct regulation of *Wnt2* and *Wnt5a*. Peak marks: blue and red squares demarcate called peaks. Dotted rectangle highlight peaks with peak marks.
(**L**) QPCR showing significant reduction in *Wnt2* mRNA upon removal of d10 $Sox9^{on\text{-}on}$ activity.
Statistical test: unpaired Student's t-test, 2-tailed, mean ± SEM.
(M) Identification of factors that might differentially cooperate with Sox9 in $Sox9^{on\text{-}on}$ cells in contrast with $Sox9^{on}$ in CUT&RUN assays.

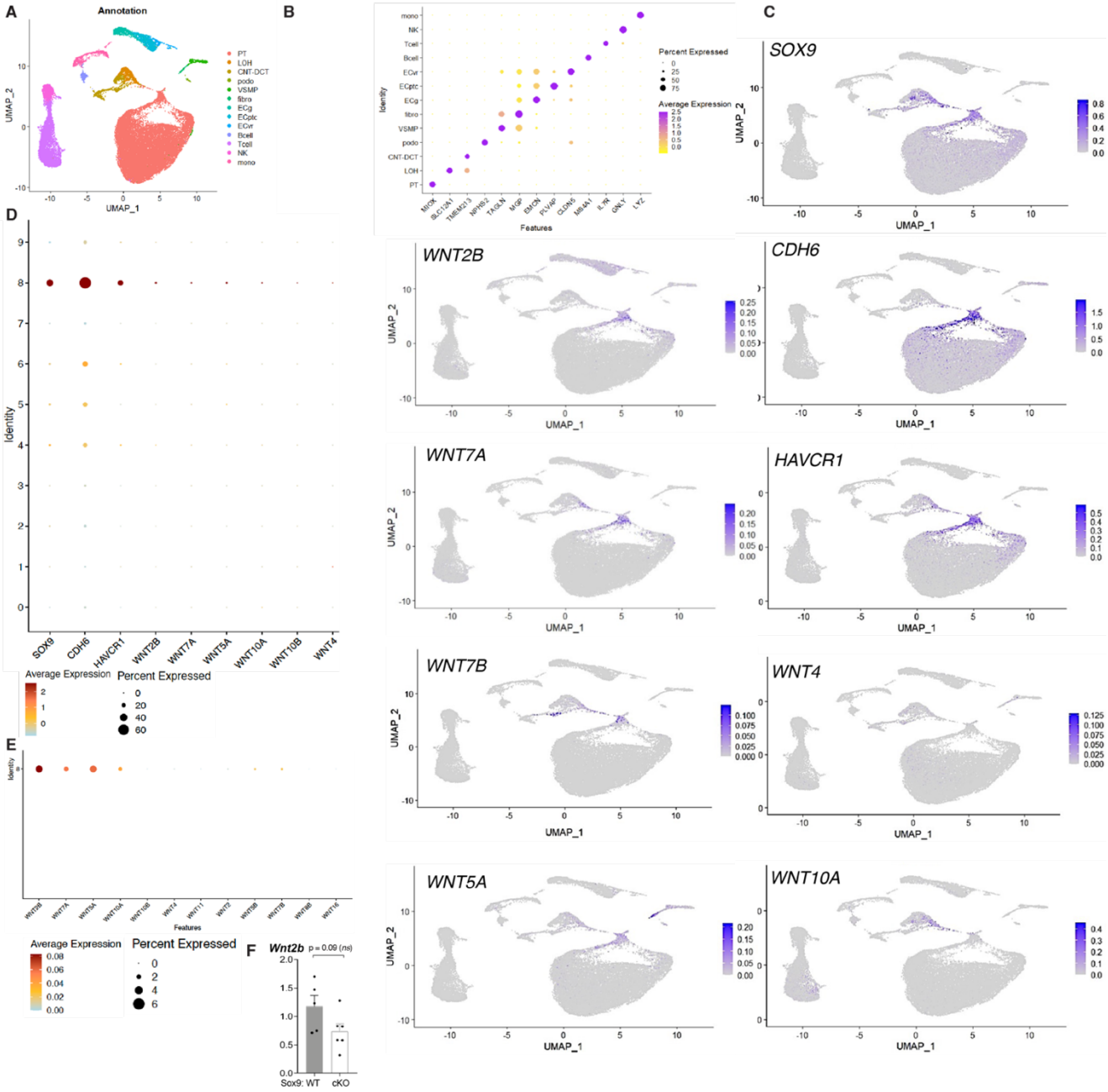

Figure S22. Single-cell level relationship of *SOX9/CDH6* and *WNT*s in human kidney transplants.

(A) UMAP showing the kidney cell types identified based on single cells RNA sequencing data of human allografts kidney biopsies (n=16).

(B) Dot plot showing average gene expression values and percentage of cells expressing the selected markers to identify major cell types. Proximal tubule (PT), Loop of Henle (LOH), podocytes (podo), vascular smooth muscle and pericytes (vSMP), fibroblasts (fibro), connecting tubule – distal convoluted tubule (CNT-DCT), three endothelial cell subsets comprising vasa recta (ECvr), glomerular (ECg) and peritubular capillaries (ECptc), B cells, T lymphocytes , NK and myeloid cells. 29,180 genes x 39,948 cells

(C) Feature plot displaying the normalized expression transcript level for *WNT*s. Note, *WNT2B, WNT7A, WNT7B, WNT5A* expression in the *SOX9/CDH6* expressing cluster of epithelial cells.

(D, E) Dot plots showing average gene expression values and percentage of cells expressing selected *WNT*s in the PT clusters (**D**), and in cluster 8 only (***E***).

(F) QPCR showing no significant difference in *Wnt2b* expression upon removal of Sox9^{on-on} activity in mice, unlike *Wnt2*, (see **fig. S19K,L**) thus highlighting differential deployment of *Wnt2* paralogous genes in human versus mice AKI to CKD.

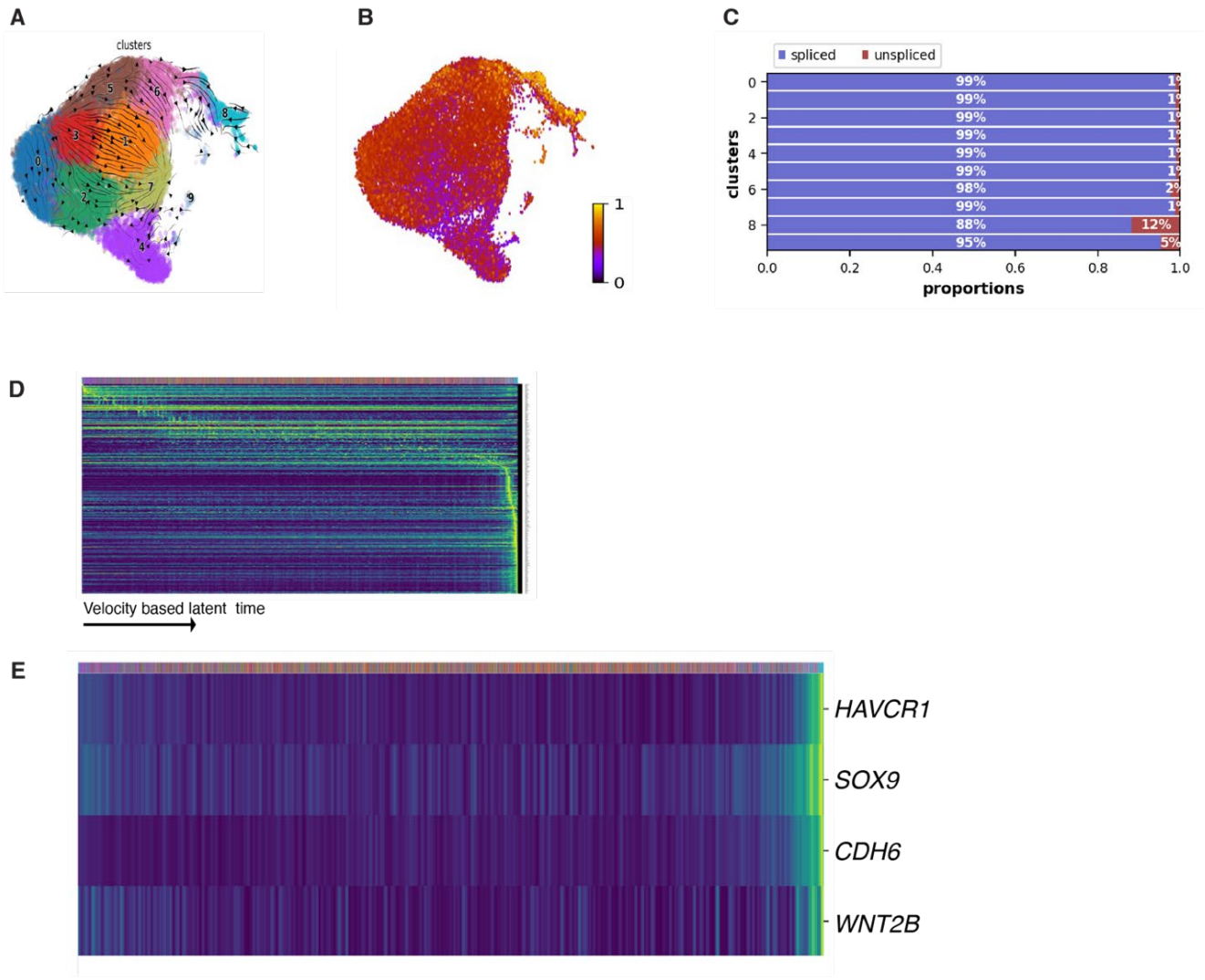

Figure S23. Cluster comprising of *SOX9/CDH6/WNT2B* expressing cells (cluster 8) in the human transplanted kidneys display dynamic transcriptional changes at the single-cell level.
(A) Velocity vector field of the subsetted proximal tubules represented as streamlines superimposed over the UMAP.
(B) Latent time of proximal tubular epithelial cells in UMAP based on dynamical modeling with scVelo demonstrating cluster 8 displays relatively greater latent time compared to other clusters.
(C) Cluster 8 displays greater proportion of unspliced/splicing mRNA counts compared to other clusters.
(D) Heatmap of top genes and their expression dynamics resolved along latent time calculated by scVelo processing, with cluster colors denoted by bar plot on top.
(E) Heatmap of subset of key genes sorted by latent time with cluster colors at top but showing enrichment in cluster 8.

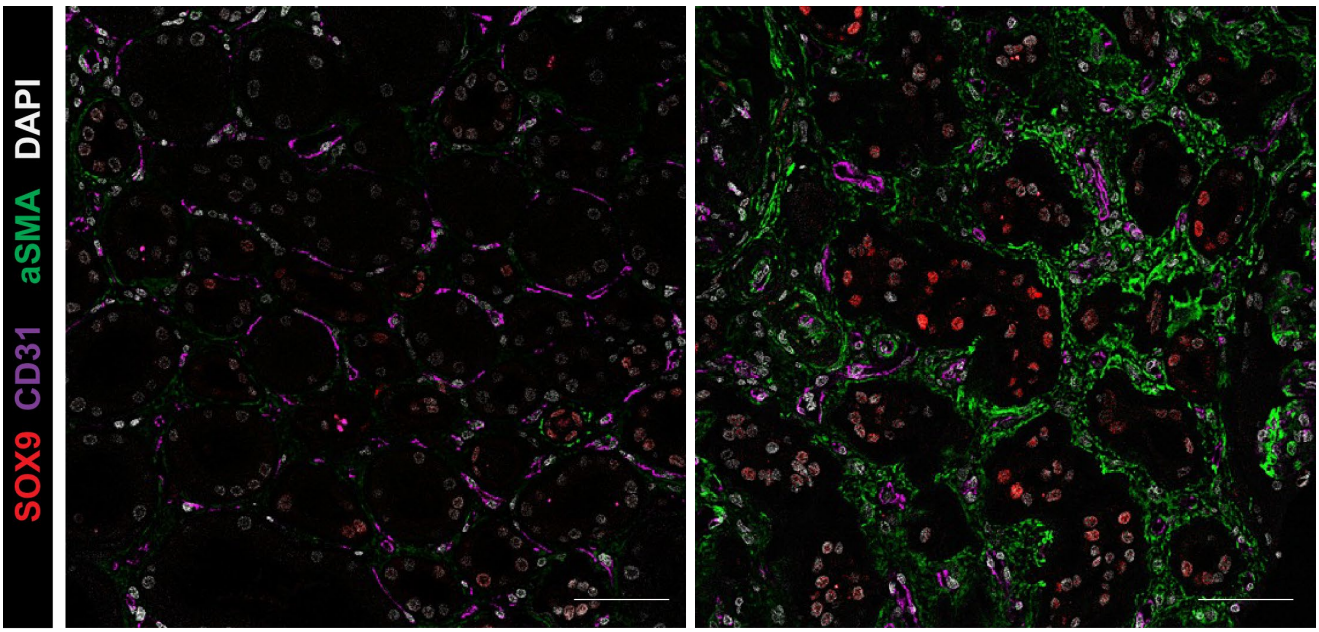

Figure S24. ACTA2 expressing myofibroblasts display intimate relationship with SOX9 expressing epithelial cells in human kidney biopsy specimen.
Representative images from the same kidney section.
Scale bars: 100μm.

Figure	Schematic	AKI to CKD Model	Cell Type	Cells Quantified
1A, H	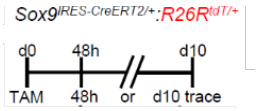	IRI	tdT+ATP1A1+	2531
			tdT+ ATP1A1neg	2153
			CDH6+ tdT+	220
1G	C57BL6 mice	IRI	CDH6+	day10: 1289
2A	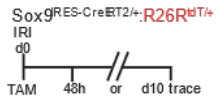	IRI	tdT+	2627
2B	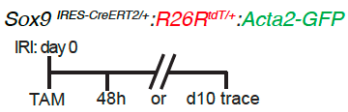	IRI	CDH6+ tdT+ GFP+	1656 2020
2J	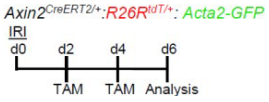	IRI	CDH6+, tdT+ GFP+	2119 1859
3A		IRI	Het (control) tdT+ tubules	616
			cKO tdT+ tubules	791
3C	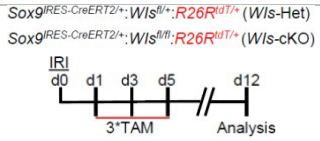	IRI	tdTneg tubules with intact *Wls*	2247
3N	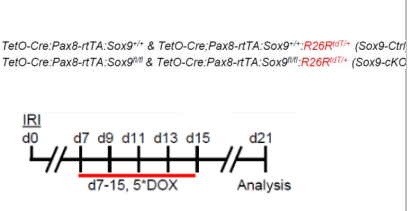	IRI	Control KIM1+ PTECs	5872
			cKO KIM1+ PTECs	5176

Table S1. The number of cells quantified in experimental cohorts.
See also corresponding main Fig. for quantification results.

Figure	Schematic	AKI to CKD Model	Cell Type	Cells Quantified
S1E to H	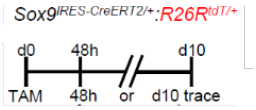	IRI	tdT+ LTL+	2534
			tdT+ LTLneg	1999
S1F	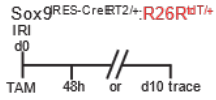	IRI	tdT+KIM1neg	1721
			tdT+KIM1+	1623
S2B	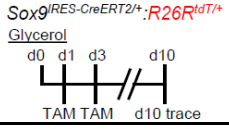	Rhabdo	tdT+ ATP1A1+	820
			tdT+ ATP1A 1neg	1071
			tdT+ LTL+	1778
			tdT+ LTLneg	2021
S7B, C	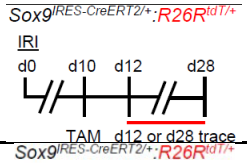	IRI day28	tdT+ATPA1+	863
			tdT+ATPA1neg	1350
			tdT+ LTL+	757
			tdT+ LTLneg	863
S10A	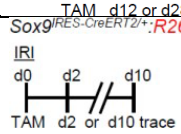	IRI	tdT+	2627
S10B	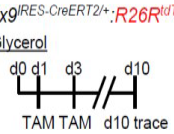	Rhabdo	tdT+	4001
S10C	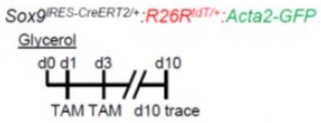	Rhabdo	tdT+	1441
S11D		IRI	tdT+	2204
S11E	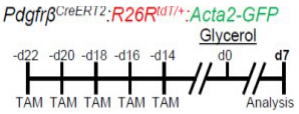	Rhabdo-	tdT+ GFP+	1285
S13A	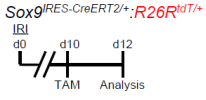	IRI	SOX9+ tdT+	1544

S13B		IRI	tdT+	1161
S14H	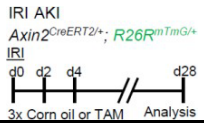	IRI AKI	mGFP+	1476
S15B	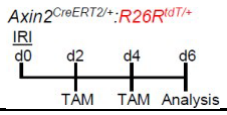	IRI	αSMA+Ki67+	527
S15C	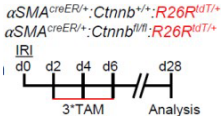	IRI	Controls tdT+ cells	4738
			cKO tdT+ cells	9504
S18B	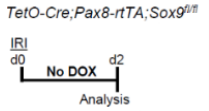	IRI	% SOX9+ Ki67+	1933

Table S2. The number of cells quantified in experimental cohorts.
See also corresponding supplemental fig. for quantification results.

tdT^{pos}GFP ^{pos} vs. tdT^{neg}GFP ^{pos}

Upregulated genes	p-value	padj. value	Downregulated genes	p-value	padj.value
Axin2	6.48E-05	0.005	*Fzd7*	0.0004	0.021
Nkd1	0.0001	0.01	*Sost*	<0.001	00.014
Dixdc1	9.48E-06	0.001	*Sfrp4*	9.48E-06	1.96E-27
Lgr6	0.0004	0.024	*Sfrp2*	0.0002	0.013
Lef1	0.001	0.042	*Wnt16*	0.0002	0.014
Apcdd1	2.21E-06	0.0004			

Table S3. Genes driving the GO term: Wnt signaling pathway in Wnt responsive cells in Fig. 3D.

Experimental Models: Organisms/Strains	SOURCE	IDENTIFIER
Mouse: *Pdgfr-b*$^{CreERT2/+}$; Tg(Pdgfrb-cre/ERT2)6096Rha/J	The Jackson Laboratory	029684
Mouse: *Axin2*$^{CreERT2/+}$; *Axin2*$^{tm1(cre/ERT2)Rnu}$/J	The Jackson Laboratory	018867
Mouse: *Slc34a1*$^{CreERT2/+}$; *Slc34a1*$^{tm1(EGFP/cre/ERT2)Bhum}$/J	The Jackson Laboratory	032285
Mouse: *LyzMCre* ; *Lyz2*$^{tm1(cre)Ifo}$/J	The Jackson Laboratory	004781
Mouse: *TetO*^{Cre} ; Tg(tetO-cre)1Jaw/J	The Jackson Laboratory	006234
Mouse: *Pax8*^{rtTA} ; Tg(Pax8-rtTA2S*M2)1Koes/J	The Jackson Laboratory	007176
Mouse: *Sox9*$^{fl/fl}$; *Sox9*^{tm2Crm}/J	The Jackson Laboratory	013106
Mouse: *Wls*$^{fl/fl}$; *Wls*$^{tm1.1Lan}$/J	The Jackson Laboratory	012888
Mouse: *Ctnnb1*$^{fl/lf}$; *Ctnnb1*^{tm2Kem}/KnwJ	The Jackson Laboratory	004152
Mouse: *R26R* $^{tdT/tdT}$; *Gt(ROSA)26Sor*$^{tm9(CAG-tdTomato)Hze}$/J	The Jackson Laboratory	007909
Mouse: *R26R* $^{mTmG/mTmG}$; *Gt(ROSA)26Sor*$^{tm4(ACTB-tdTomato,-EGFP)Luo}$/J	The Jackson Laboratory	007576
Mouse: C57BL6/J	The Jackson Laboratory	000664

Table S4. Animals from Jackson Laboratory used in this study.
For information on the *Sox9*$^{IRES-CreERT2/+}$*, Acta2-GFP,* and *Acta2*$^{CreER/+}$mouse strains, see materials and methods section under the "mouse strains" subsection.

Gene Name	Forward Primer Sequence	Reverse Primer Sequence
Actb	*TATTGGCAACGAGCGGTTC*	*CCATACCCAAGAAGGAAGGCT*
Sox9	*GAGCCGGATCTGAAGAGGGA*	*GCTTGACGTGTGGCTTGTTC*
Havcr1	*ACATATCGTGGAATCACAACGAC*	*ACAAGCAGAAGATGGGCATTG*
Wnt4	*AGACGTGCGAGAAACTCAAAG*	*GGAACTGGTATTGGCACTCCT*
Wnt7b	*TTTGGCGTCCTCTACGTGAAG*	*CCCCGATCACAATGATGGCA*
Wnt9b	*CTGGTGCTCACCTGAAGCAG*	*CCGTCTCCTTAAAGCCTCTCTG*
Wnt11	*GCTGGCACTGTCCAAGACTC*	*CTCCCGTGTACCTCTCTCCA*
Sfrp1	*CAACGTGGGCTACAAGAAGAT*	*GGCCAGTAGAAGCCGAAGAAC*
Axin2	*TGACTCTCCTTCCAGATCCCA*	*TGCCCACACTAGGCTGACA*
Col1a1	*GCTCCTCTTAGGGGCCACT*	*CCACGTCTCACCATTGGGG*
Col3a1	*ACGTAGATGAATTGGGATGCAG*	*GGGTTGGGGCAGTCTAGTG*
Acta2	*GTCCCAGACATCAGGGAGTAA*	*TCGGATACTTCAGCGTCAGGA*
Nkd1	*AGGAAAGGCATCGAGGAGTG*	*TCGCTCAGTCTCTCCATTCTC*
Nkd2	*GAGCGGAAGAAACGGACCG*	*CCTTAGGGTCTCCATTGAGCA*
Fdz7	*CGGGGCCTCAAGGAGAGAA*	*GTCCCCTAAACCGAGCCAG*
Lef1	*TGTTTATCCCATCACGGGTGG*	*CATGGAAGTGTCGCCTGACAG*
Fn1	*ATGTGGACCCCTCCTGATAGT*	*GCCCAGTGATTTCAGCAAAGG*
Wnt2	*CTCGGTGGAATCTGGCTCTG*	*CACATTGTCACACATCACCCT*
Wnt2b	*CCGACGTGTCCCCATCTTC*	*GCCCCTATGTACCACCAGGA*

Table S5. Primers used for qPCR.

Primary Antibodies	Dilution	SOURCE	IDENTIFIER
Rabbit monoclonal anti-SOX9	1:1000	Abcam	Cat# ab185230, RRID:AB_2715497
Goat polyclonal anti-KIM1	1:500	R&D Systems	Cat# AF1817, RRID:AB_2116446
Mouse monoclonal anti-ATP1A1	1:500	Abcam	Cat# ab7671, RRID:AB_306023
LTL-Biotinylated	1:1000	Vector Laboratories	Cat#B-1352-2
LTL-FITC	1:1000	Vector Laboratories	Cat#FL-1321-2
Rat monoclonal anti-Ki67	1:500	Life Technologies	Cat# 14-5698-82, RRID:AB_10854564
Rat monoclonal anti-WNT4	1:500	R&D Systems	Cat# MAB4751, RRID:AB_2215448
Mouse monoclonal anti-αSMA	1:1000	Sigma-Aldrich	Cat# A2547, RRID:AB_476701
Mouse monoclonal anti-αSMA-FITC	1:1000	Sigma-Aldrich	Cat# F3777, RRID:AB_476977
Rabbit recombinant anti-PDGFRβ	1:500	Abcam	Cat# ab32570, RRID:AB_777165
Mouse monoclonal anti-F4/80	1:100	Life Technologies	Cat# 14-4801-82, RRID:AB_467558
Rabbit recombinant anti-AQP1	1:100	Santa Cruz Biotechnology	Cat# sc-25287, RRID:AB_626694
Rat monoclonal anti-ZO-1	1:50	Life Technologies	Cat# 14-9776-82, RRID:AB_2573026
Chicken polyclonal anti-GFP	1:500	Aves Labs	Cat# GFP-1020, RRID:AB_10000240
Rabbit polyclonal anti-CDH6	1:500	Sigma	Cat# HPA007047 RRID:AB_1078374
Mouse monoclonal anti-CDH6	1:500	R&D systems	Cat# MAB-2715 RRID:AB_907139
Mouse monoclonal anti-Megalin	1:500	Santa Cruz Biotech	Cat# sc-515772 RRID:AB_2783023
Rabbit polyclonal anti-SMARCC1/Baf155	1:500	Cell Signaling Technologies	Cat# 11956
Mouse monoclonal anti-RUNX1	1:500	Santa Cruz Biotech	Cat# sc-365644

Table S6. Primary antibodies used in this study.

Secondary Antibodies	Dilution	SOURCE	IDENTIFIER
Donkey-anti-Rabbit- Alexa Fluor®488	1:1000	Life Technologies	Cat# A-21206, RRID:AB_2535792
Donkey-anti-Rabbit Alexa Fluor®555	1:1000	Life Technologies	Cat# A-31572, RRID:AB_162543
Donkey-anti-Rabbit Alexa Fluor®647	1:500	Jackson Immuno Research	Cat# 711-605-152, RRID:AB_2492288
Donkey-anti-Rat Alexa Fluor®488	1:1000	Life Technologies	Cat# A-21208, RRID:AB_2535794
Goat-anti-Rat Alexa Fluor®555	1:1000	Life Technologies	Cat# A-21434, RRID:AB_2535855
Donkey-anti-Rat-Alexa Fluor®647	1:500	Jackson Immuno Research	Cat# 712-605-153, RRID:AB_2340694
Donkey-anti-Goat Alexa Fluor®555	1:1000	Life Technologies	Cat# A-21432, RRID:AB_2535853
Donkey-anti-Goat Alexa Fluor®633	1:1000	Life Technologies	Cat# A21082, RRID:AB_10562400
Donkey-anti-Chicken Alexa Fluor®488	1:1000	Life Technologies	Cat# A-11039, RRID:AB_2534096
Goat-anti-Mouse IgG1 Alexa Fluor®488	1:1000	Life Technologies	Cat# A-21121, RRID:AB_2535764
Goat-anti-Mouse IgG2a Alexa Fluor®488	1:1000	Life Technologies	Cat# A-21131, RRID:AB_2535771
Streptavidin Alexa Fluor®647	1:1000	Life Technologies	S32357

Table S7. Secondary antibodies used in this study.

References and Notes

1. D. C. Rockey, P. D. Bell, J. A. Hill, Fibrosis—A common pathway to organ injury and failure. *N. Engl. J. Med.* **372**, 1138–1149 (2015). doi:10.1056/NEJMra1300575 Medline

2. N. C. Henderson, F. Rieder, T. A. Wynn, Fibrosis: From mechanisms to medicines. *Nature* **587**, 555–566 (2020). doi:10.1038/s41586-020-2938-9 Medline

3. P. Konieczny, S. Naik, Healing without scarring. *Science* **372**, 346–347 (2021). doi:10.1126/science.abi5770 Medline

4. S. Kumar, Cellular and molecular pathways of renal repair after acute kidney injury. *Kidney Int.* **93**, 27–40 (2018). doi:10.1016/j.kint.2017.07.030 Medline

5. J. Liu, S. Kumar, E. Dolzhenko, G. F. Alvarado, J. Guo, C. Lu, Y. Chen, M. Li, M. C. Dessing, R. K. Parvez, P. E. Cippà, A. M. Krautzberger, G. Saribekyan, A. D. Smith, A. P. McMahon, Molecular characterization of the transition from acute to chronic kidney injury following ischemia/reperfusion. *JCI Insight* **2**, e94716 (2017). doi:10.1172/jci.insight.94716 Medline

6. J. G. Abuelo, Normotensive ischemic acute renal failure. *N. Engl. J. Med.* **357**, 797–805 (2007). doi:10.1056/NEJMra064398 Medline

7. J. V. Bonventre, L. Yang, Cellular pathophysiology of ischemic acute kidney injury. *J. Clin. Invest.* **121**, 4210–4221 (2011). doi:10.1172/JCI45161 Medline

8. I. Grgic, G. Campanholle, V. Bijol, C. Wang, V. S. Sabbisetti, T. Ichimura, B. D. Humphreys, J. V. Bonventre, Targeted proximal tubule injury triggers interstitial fibrosis and glomerulosclerosis. *Kidney Int.* **82**, 172–183 (2012). doi:10.1038/ki.2012.20 Medline

9. M. A. Venkatachalam, K. A. Griffin, R. Lan, H. Geng, P. Saikumar, A. K. Bidani, Acute kidney injury: A springboard for progression in chronic kidney disease. *Am. J. Physiol. Renal Physiol.* **298**, F1078–F1094 (2010). doi:10.1152/ajprenal.00017.2010 Medline

10. S. Kumar, J. Liu, P. Pang, A. M. Krautzberger, A. Reginensi, H. Akiyama, A. Schedl, B. D. Humphreys, A. P. McMahon, Sox9 activation highlights a cellular pathway of renal repair in the acutely injured mammalian kidney. *Cell Rep.* **12**, 1325–1338 (2015). doi:10.1016/j.celrep.2015.07.034 Medline

11. K. Zhang, S. Chen, H. Sun, L. Wang, H. Li, J. Zhao, C. Zhang, N. Li, Z. Guo, Z. Han, Z.-C. Han, G. Zheng, X. Chen, Z. Li, *In vivo* two-photon microscopy reveals the contribution of $Sox9^{+}$ cell to kidney regeneration in a mouse model with extracellular vesicle treatment. *J. Biol. Chem.* **295**, 12203–12213 (2020). doi:10.1074/jbc.RA120.012732 Medline

12. B. L. Hogan, P. A. Kolodziej, Organogenesis: Molecular mechanisms of tubulogenesis. *Nat. Rev. Genet.* **3**, 513–523 (2002). doi:10.1038/nrg840 Medline

13. W. J. Nelson, R. Nusse, Convergence of Wnt, beta-catenin, and cadherin pathways. *Science* **303**, 1483–1487 (2004). doi:10.1126/science.1094291 Medline

14. V. Vasioukhin, C. Bauer, M. Yin, E. Fuchs, Directed actin polymerization is the driving force for epithelial cell-cell adhesion. *Cell* **100**, 209–219 (2000). doi:10.1016/S0092-8674(00)81559-7 Medline

15. S. P. Mah, H. Saueressig, M. Goulding, C. Kintner, G. R. Dressler, Kidney development in cadherin-6 mutants: Delayed mesenchyme-to-epithelial conversion and loss of nephrons. *Dev. Biol.* **223**, 38–53 (2000). doi:10.1006/dbio.2000.9738 Medline

16. S. Thelen, M. Abouhamed, G. Ciarimboli, B. Edemir, M. Bähler, Rho GAP myosin IXa is a regulator of kidney tubule function. *Am. J. Physiol. Renal Physiol.* **309**, F501–F513 (2015). doi:10.1152/ajprenal.00220.2014 Medline

17. Y. Kirita, H. Wu, K. Uchimura, P. C. Wilson, B. D. Humphreys, Cell profiling of mouse acute kidney injury reveals conserved cellular responses to injury. *Proc. Natl. Acad. Sci. U.S.A.* **117**, 15874–15883 (2020). doi:10.1073/pnas.2005477117 Medline

18. D. Legouis, S.-E. Ricksten, A. Faivre, T. Verissimo, K. Gariani, C. Verney, P. Galichon, L. Berchtold, E. Feraille, M. Fernandez, S. Placier, K. Koppitch, A. Hertig, P.-Y. Martin, M. Naesens, J. Pugin, A. P. McMahon, P. E. Cippà, S. de Seigneux, Altered proximal tubular cell glucose metabolism during acute kidney injury is associated with mortality. *Nat. Metab.* **2**, 732–743 (2020). doi:10.1038/s42255-020-0238-1 Medline

19. Y. Neirijnck, A. Reginensi, K. Y. Renkema, F. Massa, V. M. Kozlov, H. Dhib, E. M. H. F. Bongers, W. F. Feitz, A. M. van Eerde, V. Lefebvre, N. V. A. M. Knoers, M. Tabatabaei, H. Schulz, H. McNeill, F. Schaefer, M. Wegner, E. Sock, A. Schedl, Sox11 gene disruption causes congenital anomalies of the kidney and urinary tract (CAKUT). *Kidney Int.* **93**, 1142–1153 (2018). doi:10.1016/j.kint.2017.11.026 Medline

20. H. Clevers, K. M. Loh, R. Nusse, An integral program for tissue renewal and regeneration: Wnt signaling and stem cell control. *Science* **346**, 1248012 (2014). doi:10.1126/science.1248012 Medline

21. H. F. Farin, I. Jordens, M. H. Mosa, O. Basak, J. Korving, D. V. F. Tauriello, K. de Punder, S. Angers, P. J. Peters, M. M. Maurice, H. Clevers, Visualization of a short-range Wnt gradient in the intestinal stem-cell niche. *Nature* **530**, 340–343 (2016). doi:10.1038/nature16937 Medline

22. B. Degirmenci, T. Valenta, S. Dimitrieva, G. Hausmann, K. Basler, GLI1-expressing mesenchymal cells form the essential Wnt-secreting niche for colon stem cells. *Nature* **558**, 449–453 (2018). doi:10.1038/s41586-018-0190-3 Medline

23. S. Kim, H. Nie, V. Nesin, U. Tran, P. Outeda, C.-X. Bai, J. Keeling, D. Maskey, T. Watnick, O. Wessely, L. Tsiokas, The polycystin complex mediates Wnt/Ca(2+) signalling. *Nat. Cell Biol.* **18**, 752–764 (2016). doi:10.1038/ncb3363 Medline

24. Y. Rinkevich, D. T. Montoro, H. Contreras-Trujillo, O. Harari-Steinberg, A. M. Newman, J. M. Tsai, X. Lim, R. Van-Amerongen, A. Bowman, M. Januszyk, O. Pleniceanu, R. Nusse, M. T. Longaker, I. L. Weissman, B. Dekel, In vivo clonal

analysis reveals lineage-restricted progenitor characteristics in mammalian kidney development, maintenance, and regeneration. *Cell Rep.* **7**, 1270–1283 (2014). doi:10.1016/j.celrep.2014.04.018 Medline

25. C. Bänziger, D. Soldini, C. Schütt, P. Zipperlen, G. Hausmann, K. Basler, Wntless, a conserved membrane protein dedicated to the secretion of Wnt proteins from signaling cells. *Cell* **125**, 509–522 (2006). doi:10.1016/j.cell.2006.02.049 Medline

26. D. P. DiRocco, A. Kobayashi, M. M. Taketo, A. P. McMahon, B. D. Humphreys, Wnt4/β-catenin signaling in medullary kidney myofibroblasts. *J. Am. Soc. Nephrol.* **24**, 1399–1412 (2013). doi:10.1681/ASN.2012050512 Medline

27. C. Kuppe, M. M. Ibrahim, J. Kranz, X. Zhang, S. Ziegler, J. Perales-Patón, J. Jansen, K. C. Reimer, J. R. Smith, R. Dobie, J. R. Wilson-Kanamori, M. Halder, Y. Xu, N. Kabgani, N. Kaesler, M. Klaus, L. Gernhold, V. G. Puelles, T. B. Huber, P. Boor, S. Menzel, R. M. Hoogenboezem, E. M. J. Bindels, J. Steffens, J. Floege, R. K. Schneider, J. Saez-Rodriguez, N. C. Henderson, R. Kramann, Decoding myofibroblast origins in human kidney fibrosis. *Nature* **589**, 281–286 (2021). doi:10.1038/s41586-020-2941-1 Medline

28. W. Guo, Z. Keckesova, J. L. Donaher, T. Shibue, V. Tischler, F. Reinhardt, S. Itzkovitz, A. Noske, U. Zürrer-Härdi, G. Bell, W. L. Tam, S. A. Mani, A. van Oudenaarden, R. A. Weinberg, Slug and Sox9 cooperatively determine the mammary stem cell state. *Cell* **148**, 1015–1028 (2012). doi:10.1016/j.cell.2012.02.008 Medline

29. C. López-Rodríguez, C. L. Antos, J. M. Shelton, J. A. Richardson, F. Lin, T. I. Novobrantseva, R. T. Bronson, P. Igarashi, A. Rao, E. N. Olson, Loss of NFAT5 results in renal atrophy and lack of tonicity-responsive gene expression. *Proc. Natl. Acad. Sci. U.S.A.* **101**, 2392–2397 (2004). doi:10.1073/pnas.0308703100 Medline

30. M. Haller, J. Au, M. O'Neill, D. J. Lamb, 16p11.2 transcription factor *MAZ* is a dosage-sensitive regulator of genitourinary development. *Proc. Natl. Acad. Sci. U.S.A.* **115**, E1849–E1858 (2018). doi:10.1073/pnas.1716092115 Medline

31. M. Bouchard, A. Souabni, M. Mandler, A. Neubüser, M. Busslinger, Nephric lineage specification by Pax2 and Pax8. *Genes Dev.* **16**, 2958–2970 (2002). doi:10.1101/gad.240102 Medline

32. L. Ho, J. L. Ronan, J. Wu, B. T. Staahl, L. Chen, A. Kuo, J. Lessard, A. I. Nesvizhskii, J. Ranish, G. R. Crabtree, An embryonic stem cell chromatin remodeling complex, esBAF, is essential for embryonic stem cell self-renewal and pluripotency. *Proc. Natl. Acad. Sci. U.S.A.* **106**, 5181–5186 (2009). doi:10.1073/pnas.0812889106 Medline

33. P. Li, J. L. Lahvic, V. Binder, E. K. Pugach, E. B. Riley, O. J. Tamplin, D. Panigrahy, T. V. Bowman, F. G. Barrett, G. C. Heffner, S. McKinney-Freeman, T. M. Schlaeger, G. Q. Daley, D. C. Zeldin, L. I. Zon, Epoxyeicosatrienoic acids enhance embryonic haematopoiesis and adult marrow engraftment. *Nature* **523**, 468–471 (2015). doi:10.1038/nature14569 Medline

34. S. Ohba, X. He, H. Hojo, A. P. McMahon, Distinct Transcriptional Programs Underlie Sox9 Regulation of the Mammalian Chondrocyte. *Cell Rep.* **12**, 229–243 (2015). doi:10.1016/j.celrep.2015.06.013 Medline

35. B. M. Fuglerud, S. Drissler, J. Lotto, T. L. Stephan, A. Thakur, R. Cullum, P. A. Hoodless, SOX9 reprograms endothelial cells by altering the chromatin landscape. *Nucleic Acids Res.* **50**, 8547–8565 (2022). doi:10.1093/nar/gkac652 Medline

36. V. R. Harley, R. Lovell-Badge, P. N. Goodfellow, P. J. Hextall, The HMG box of SRY is a calmodulin binding domain. *FEBS Lett.* **391**, 24–28 (1996). doi:10.1016/0014-5793(96)00694-1 Medline

37. A. Argentaro, H. Sim, S. Kelly, S. Preiss, A. Clayton, D. A. Jans, V. R. Harley, A SOX9 defect of calmodulin-dependent nuclear import in campomelic dysplasia/autosomal sex reversal. *J. Biol. Chem.* **278**, 33839–33847 (2003). doi:10.1074/jbc.M302078200 Medline

38. N. van Gastel, S. Stegen, G. Eelen, S. Schoors, A. Carlier, V. W. Daniëls, N. Baryawno, D. Przybylski, M. Depypere, P.-J. Stiers, D. Lambrechts, R. Van Looveren, S. Torrekens, A. Sharda, P. Agostinis, D. Lambrechts, F. Maes, J. V. Swinnen, L. Geris, H. Van Oosterwyck, B. Thienpont, P. Carmeliet, D. T. Scadden, G. Carmeliet, Lipid availability determines fate of skeletal progenitor cells via SOX9. *Nature* **579**, 111–117 (2020). doi:10.1038/s41586-020-2050-1 Medline

39. F. Liu, G. C. Hon, G. R. Villa, K. M. Turner, S. Ikegami, H. Yang, Z. Ye, B. Li, S. Kuan, A. Y. Lee, C. Zanca, B. Wei, G. Lucey, D. Jenkins, W. Zhang, C. L. Barr, F. B. Furnari, T. F. Cloughesy, W. H. Yong, T. C. Gahman, A. K. Shiau, W. K. Cavenee, B. Ren, P. S. Mischel, EGFR Mutation Promotes Glioblastoma through Epigenome and Transcription Factor Network Remodeling. *Mol. Cell* **60**, 307–318 (2015). doi:10.1016/j.molcel.2015.09.002 Medline

40. D. M. Bell, K. K. H. Leung, S. C. Wheatley, L. J. Ng, S. Zhou, K. W. Ling, M. H. Sham, P. Koopman, P. P. L. Tam, K. S. E. Cheah, SOX9 directly regulates the type-II collagen gene. *Nat. Genet.* **16**, 174–178 (1997). doi:10.1038/ng0697-174 Medline

41. C. D. Oh, S. N. Maity, J.-F. Lu, J. Zhang, S. Liang, F. Coustry, B. de Crombrugghe, H. Yasuda, Identification of SOX9 interaction sites in the genome of chondrocytes. *PLOS ONE* **5**, e10113 (2010). doi:10.1371/journal.pone.0010113 Medline

42. P. A. Seymour, H. P. Shih, N. A. Patel, K. K. Freude, R. Xie, C. J. Lim, M. Sander, A Sox9/Fgf feed-forward loop maintains pancreatic organ identity. *Development* **139**, 3363–3372 (2012). doi:10.1242/dev.078733 Medline

43. Q. Guo, A. Kim, B. Li, A. Ransick, H. Bugacov, X. Chen, N. Lindström, A. Brown, L. Oxburgh, B. Ren, A. P. McMahon, A β-catenin-driven switch in TCF/LEF transcription factor binding to DNA target sites promotes commitment of mammalian nephron progenitor cells. *eLife* **10**, e64444 (2021). doi:10.7554/eLife.64444 Medline

44. A. S. Weintraub, C. H. Li, A. V. Zamudio, A. A. Sigova, N. M. Hannett, D. S. Day, B. J. Abraham, M. A. Cohen, B. Nabet, D. L. Buckley, Y. E. Guo, D. Hnisz, R. Jaenisch, J. E. Bradner, N. S. Gray, R. A. Young, YY1 is a structural regulator of enhancer-promoter loops. *Cell* **171**, 1573–1588.e28 (2017). doi:10.1016/j.cell.2017.11.008 Medline

45. H. Nguyen, B. J. Merrill, L. Polak, M. Nikolova, M. Rendl, T. M. Shaver, H. A. Pasolli, E. Fuchs, Tcf3 and Tcf4 are essential for long-term homeostasis of skin epithelia. *Nat. Genet.* **41**, 1068–1075 (2009). doi:10.1038/ng.431 Medline

46. J. C. Robins, N. Akeno, A. Mukherjee, R. R. Dalal, B. J. Aronow, P. Koopman, T. L. Clemens, Hypoxia induces chondrocyte-specific gene expression in mesenchymal cells in association with transcriptional activation of Sox9. *Bone* **37**, 313–322 (2005). doi:10.1016/j.bone.2005.04.040 Medline

47. E. Huang, A. Vo, J. Choi, N. Ammerman, K. Lim, S. Sethi, I. Kim, S. Kumar, R. Najjar, A. Peng, S. C. Jordan, Three-year outcomes of a randomized, double-blind, placebo-controlled study assessing safety and efficacy of C1 esterase inhibitor for prevention of delayed graft function in deceased donor kidney transplant recipients. *Clin. J. Am. Soc. Nephrol.* **15**, 109–116 (2020). doi:10.2215/CJN.04840419 Medline

48. P. E. Cippà, J. Liu, B. Sun, S. Kumar, M. Naesens, A. P. McMahon, A late B lymphocyte action in dysfunctional tissue repair following kidney injury and transplantation. *Nat. Commun.* **10**, 1157 (2019). doi:10.1038/s41467-019-09092-2 Medline

49. P. E. Cippà, B. Sun, J. Liu, L. Chen, M. Naesens, A. P. McMahon, Transcriptional trajectories of human kidney injury progression. *JCI Insight* **3**, e123151 (2018). doi:10.1172/jci.insight.123151 Medline

50. B. Lamarthée, J. Callemeyn, Y. Van Herck, A. Antoranz, D. Anglicheau, P. Boada, J. U. Becker, T. Debyser, F. De Smet, K. De Vusser, M. Eloudzeri, A. Franken, W. Gwinner, P. Koshy, D. Kuypers, D. Lambrechts, P. Marquet, V. Mathias, M. Rabant, M. M. Sarwal, A. Senev, T. K. Sigdel, B. Sprangers, O. Thaunat, C. Tinel, T. Van Brussel, A. Van Craenenbroeck, E. Van Loon, T. Vaulet, F. Bosisio, M. Naesens, Transcriptional and spatial profiling of the kidney allograft unravels a central role for FcyRIII+ innate immune cells in rejection. *Nat. Commun.* **14**, 4359 (2023). doi:10.1038/s41467-023-39859-7 Medline

51. B. D. Humphreys, Mechanisms of renal fibrosis. *Annu. Rev. Physiol.* **80**, 309–326 (2018). doi:10.1146/annurev-physiol-022516-034227 Medline

52. O. Burgy, M. Königshoff, The WNT signaling pathways in wound healing and fibrosis. *Matrix Biol.* **68-69**, 67–80 (2018). doi:10.1016/j.matbio.2018.03.017 Medline

53. L. Yang, T. Y. Besschetnova, C. R. Brooks, J. V. Shah, J. V. Bonventre, Epithelial cell cycle arrest in G2/M mediates kidney fibrosis after injury. *Nat. Med.* **16**, 535–543, 1p, 143 (2010). doi:10.1038/nm.2144 Medline

54. J. M. Wolstein, D. H. Lee, J. Michaud, V. Buot, B. Stefanchik, M. D. Plotkin, INK4a knockout mice exhibit increased fibrosis under normal conditions and in response to unilateral ureteral obstruction. *Am. J. Physiol. Renal Physiol.* **299**, F1486–F1495 (2010). doi:10.1152/ajprenal.00378.2010 Medline

55. S. Raza, E. Jokl, J. Pritchett, K. Martin, K. Su, K. Simpson, L. Birchall, A. F. Mullan, V. S. Athwal, D. T. Doherty, L. Zeef, N. C. Henderson, P. A. Kalra, N. A. Hanley, K. Piper Hanley, SOX9 is required for kidney fibrosis and activates NAV3 to drive renal myofibroblast function. *Sci. Signal.* **14**, eabb4282 (2021). doi:10.1126/scisignal.abb4282 Medline

56. C. Ricci-Tam, I. Ben-Zion, J. Wang, J. Palme, A. Li, Y. Savir, M. Springer, Decoupling transcription factor expression and activity enables dimmer switch gene regulation. *Science* **372**, 292–295 (2021). doi:10.1126/science.aba7582 Medline

57. I. Vasic, A. R. G. Libby, A. Maslan, E. A. Bulger, D. Zalazar, M. Z. Krakora Compagno, A. Streets, K. Tomoda, S. Yamanaka, T. C. McDevitt, Loss of TJP1 disrupts gastrulation patterning and increases differentiation toward the germ cell lineage in human pluripotent stem cells. *Dev. Cell* **58**, 1477–1488.e5 (2023). doi:10.1016/j.devcel.2023.05.019 Medline

58. K. Furuyama, Y. Kawaguchi, H. Akiyama, M. Horiguchi, S. Kodama, T. Kuhara, S. Hosokawa, A. Elbahrawy, T. Soeda, M. Koizumi, T. Masui, M. Kawaguchi, K. Takaori, R. Doi, E. Nishi, R. Kakinoki, J. M. Deng, R. R. Behringer, T. Nakamura, S. Uemoto, Continuous cell supply from a Sox9-expressing progenitor zone in adult liver, exocrine pancreas and intestine. *Nat. Genet.* **43**, 34–41 (2011). doi:10.1038/ng.722 Medline

59. T. Xie, J. Liang, N. Liu, C. Huan, Y. Zhang, W. Liu, M. Kumar, R. Xiao, J. D'Armiento, D. Metzger, P. Chambon, V. E. Papaioannou, B. R. Stripp, D. Jiang, P. W. Noble, Transcription factor TBX4 regulates myofibroblast accumulation and lung fibrosis. *J. Clin. Invest.* **126**, 3063–3079 (2016). doi:10.1172/JCI85328 Medline

60. A. B. Condren, A. Kumar, P. Mettu, K. J. Liang, L. Zhao, J. Y. Tsai, R. N. Fariss, W. T. Wong, Perivascular mural cells of the mouse choroid demonstrate morphological diversity that is correlated to vasoregulatory function. *PLOS ONE* **8**, e53386 (2013). doi:10.1371/journal.pone.0053386 Medline

61. O. Wendling, J. M. Bornert, P. Chambon, D. Metzger, Efficient temporally-controlled targeted mutagenesis in smooth muscle cells of the adult mouse. *Genesis* **47**, 14–18 (2009). doi:10.1002/dvg.20448 Medline

62. M. Adam, A. S. Potter, S. S. Potter, Psychrophilic proteases dramatically reduce single-cell RNA-seq artifacts: A molecular atlas of kidney development. *Development* **144**, 3625–3632 (2017). doi:10.1242/dev.151142 Medline

63. A. Dobin, C. A. Davis, F. Schlesinger, J. Drenkow, C. Zaleski, S. Jha, P. Batut, M. Chaisson, T. R. Gingeras, STAR: Ultrafast universal RNA-seq aligner. *Bioinformatics* **29**, 15–21 (2013). doi:10.1093/bioinformatics/bts635 Medline

64. Y. Hao, S. Hao, E. Andersen-Nissen, W. M. Mauck 3rd, S. Zheng, A. Butler, M. J. Lee, A. J. Wilk, C. Darby, M. Zager, P. Hoffman, M. Stoeckius, E. Papalexi, E. P. Mimitou, J. Jain, A. Srivastava, T. Stuart, L. M. Fleming, B. Yeung, A. J. Rogers, J. M. McElrath, C. A. Blish, R. Gottardo, P. Smibert, R. Satija, Integrated analysis of multimodal single-cell data. *Cell* **184**, 3573–3587.e29 (2021). doi:10.1016/j.cell.2021.04.048 Medline

65. B. B. Lake, R. Menon, S. Winfree, Q. Hu, R. Melo Ferreira, K. Kalhor, D. Barwinska, E. A. Otto, M. Ferkowicz, D. Diep, N. Plongthongkum, A. Knoten, S. Urata, L. H. Mariani, A. S. Naik, S. Eddy, B. Zhang, Y. Wu, D. Salamon, J. C. Williams, X. Wang, K. S. Balderrama, P. J. Hoover, E. Murray, J. L. Marshall, T. Noel, A. Vijayan, A. Hartman, F. Chen, S. S. Waikar, S. E. Rosas, F. P. Wilson, P. M. Palevsky, K. Kiryluk, J. R. Sedor, R. D. Toto, C. R. Parikh, E. H. Kim, R. Satija, A. Greka, E. Z. Macosko, P. V. Kharchenko, J. P. Gaut, J. B. Hodgin, KPMP Consortium, M. T. Eadon, P. C. Dagher, T. M. El-Achkar, K. Zhang, M. Kretzler, S. Jain, An atlas of healthy and injured cell states and niches in the human kidney. *Nature* **619**, 585–594 (2023). doi:10.1038/s41586-023-05769-3 Medline

66. T. Wu, E. Hu, S. Xu, M. Chen, P. Guo, Z. Dai, T. Feng, L. Zhou, W. Tang, L. Zhan, X. Fu, S. Liu, X. Bo, G. Yu, clusterProfiler 4.0: A universal enrichment tool for interpreting omics data. *Innovation (Camb.)* **2**, 100141 (2021). doi:10.1016/j.xinn.2021.100141 Medline

67. J. M. Granja, M. R. Corces, S. E. Pierce, S. T. Bagdatli, H. Choudhry, H. Y. Chang, W. J. Greenleaf, ArchR is a scalable software package for integrative single-cell chromatin accessibility analysis. *Nat. Genet.* **53**, 403–411 (2021). doi:10.1038/s41588-021-00790-6 Medline

68. D. van Dijk, R. Sharma, J. Nainys, K. Yim, P. Kathail, A. J. Carr, C. Burdziak, K. R. Moon, C. L. Chaffer, D. Pattabiraman, B. Bierie, L. Mazutis, G. Wolf, S. Krishnaswamy, D. Pe'er, Recovering gene interactions from single-cell data using data diffusion. *Cell* **174**, 716–729.e27 (2018). doi:10.1016/j.cell.2018.05.061 Medline

69. A. N. Schep, B. Wu, J. D. Buenrostro, W. J. Greenleaf, chromVAR: Inferring transcription-factor-associated accessibility from single-cell epigenomic data. *Nat. Methods* **14**, 975–978 (2017). doi:10.1038/nmeth.4401 Medline